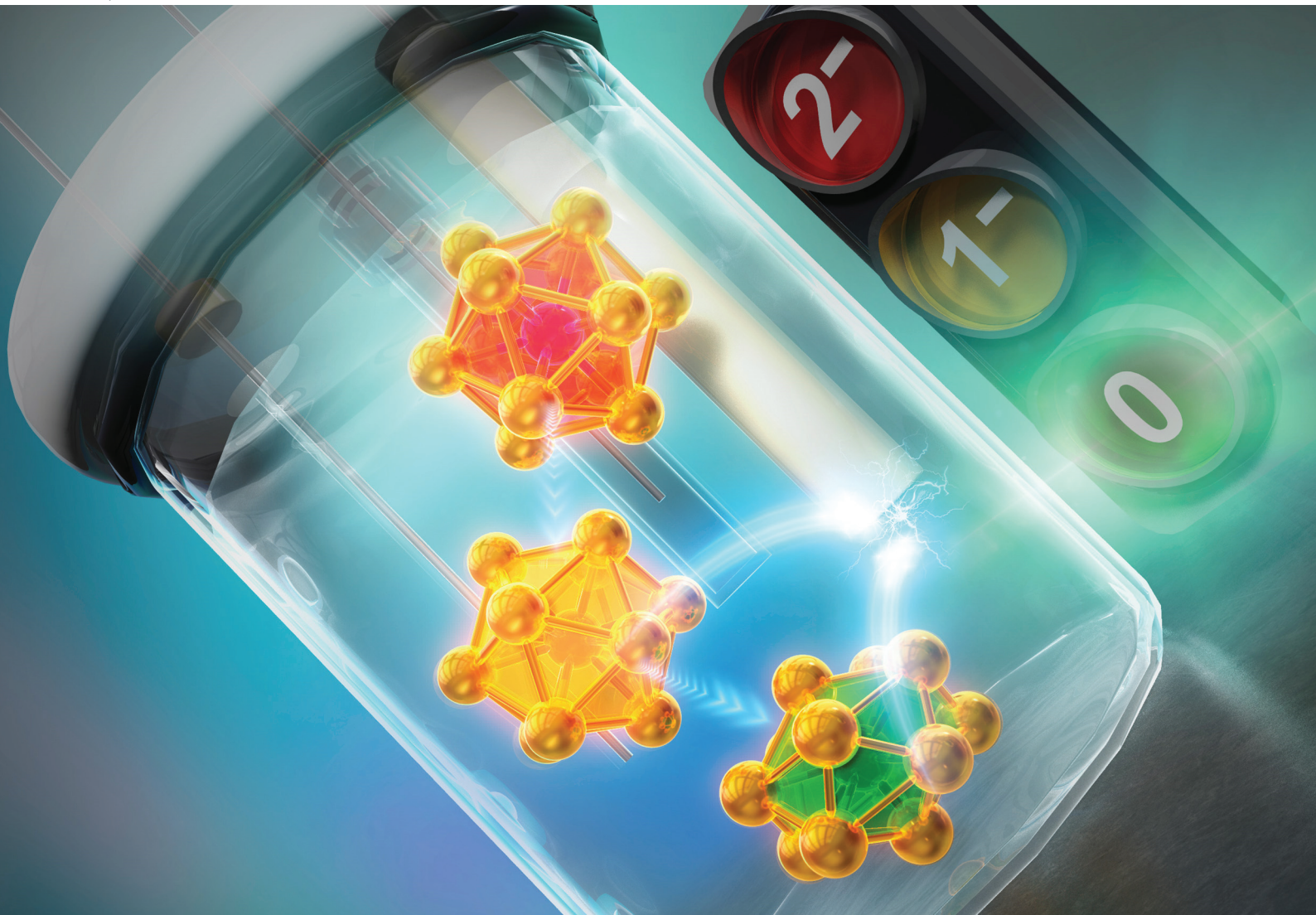


# Dalton Transactions

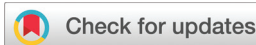
An international journal of inorganic chemistry

[rsc.li/dalton](http://rsc.li/dalton)



Themed issue: New Talent: Asia Pacific

ISSN 1477-9226



Cite this: *Dalton Trans.*, 2023, **52**, 15152

## Elucidation of the electronic structures of thiolate-protected gold nanoclusters by electrochemical measurements

Tokuhisa Kawakami <sup>a,b</sup> and Yuichi Negishi <sup>a,b</sup>

Metal nanoclusters (NCs) with sizes of approximately 2 nm or less have different physical/chemical properties from those of the bulk metals owing to quantum size effects. Metal NCs, which can be size-controlled and heterometal doped at atomic accuracy, are expected to be the next generation of important materials, and new metal NCs are reported regularly. However, compared with conventional materials such as metal complexes and relatively large metal nanoparticles (>2 nm), these metal NCs are still under-developed in terms of evaluation and establishment of application methods. Electrochemical measurements are one of the most widely used methods for synthesis, application, and characterisation of metal NCs. This review summarizes the basic knowledge of the electrochemistry and experimental techniques, and provides examples of the reported electronic states of thiolate-protected gold NCs elucidated by electrochemical approaches. It is expected that this review will provide useful information for researchers starting to study metal NCs.

Received 27th June 2023,  
Accepted 29th August 2023  
DOI: 10.1039/d3dt02005c  
[rsc.li/dalton](http://rsc.li/dalton)

<sup>a</sup>Department of Applied Chemistry, Faculty of Science, Tokyo University of Science, Kagurazaka, Shinjuku-ku, Tokyo 162-8601, Japan. E-mail: [kawakami@rs.tus.ac.jp](mailto:kawakami@rs.tus.ac.jp), [negishi@rs.tus.ac.jp](mailto:negishi@rs.tus.ac.jp)

<sup>b</sup>Research Institute for Science & Technology, Tokyo University of Science, Shinjuku-ku, Tokyo 162-8601, Japan



**Tokuhisa Kawakami**

*Tokuhisa Kawakami is a Junior Associate Professor in the Department of Applied Chemistry at Tokyo University of Science. He received his Ph.D. degree in applied chemistry from the University of Tokyo in 2015. In 2016, he worked as a Japan Society for the Promotion of Science (JSPS) postdoctoral fellow at the University of Melbourne. He then worked as a JSPS super postdoctoral fellow at Kyoto University. In 2019, he moved to his current University. His current research topics include the synthesis of ligand-protected metal nanoparticles and nanoclusters and their application in photoelectrochemistry and photocatalysis.*

## 1 Introduction

Metal nanoclusters (NCs) are a promising and widely studied group of next-generation nanomaterials.<sup>1–7</sup> Although there is no strict definition of a NC, when the size of a metal particle is below ~2 nm, it is often called a metal NC. Metal NCs are known to have different electronic/geometric structures from both the corresponding bulk metals and metal nanoparticles



**Yuichi Negishi**

*Yuichi Negishi is a professor at the Department of Applied Chemistry at TUS. He received his Ph.D. degree in chemistry (2001) from Keio University under the supervision of Prof. Atsushi Nakajima. Before joining TUS in 2008, he was employed as an assistant professor at Keio University and the Institute for Molecular Science. His current research interests include the precise synthesis of stable and functionalized metal nanoclusters, metal nanocluster-connected structures, and covalent organic frameworks.*



(NPs), and they thus have different physical properties and functions. Furthermore, because such properties and functions are dependent on the number of constituent atoms, creation of multiple functions with a single element is possible if the number of constituent atoms can be controlled in the size region of metal NCs. If multiple elements are used,<sup>8,9</sup> an even greater variety of functions can be created. Among these metal NCs, gold (Au) NCs protected by thiolate (SR) groups ( $\text{Au}_n(\text{SR})_m$ , where  $n$  is the number of constituent Au atoms and  $m$  is the number of SR ligands) have been the most studied. This is because of their simple and easy synthesis under atmospheric conditions and their relatively high chemical and thermal stability. Furthermore, many  $\text{Au}_n(\text{SR})_m$  NCs can be analysed by single-crystal X-ray diffraction (SCXRD) to reveal their geometric structure and by density functional theory (DFT) calculations to reveal their electronic structure and origin of constructed orbitals.<sup>10,11</sup> Therefore,  $\text{Au}_n(\text{SR})_m$  NCs have attracted widespread attention as novel nanomaterials in environmental, energy, and biological fields.<sup>12–17</sup>

Electrochemical methods play an important role in investigation of metal NCs with respect to elucidation of their electronic structures (Fig. 1).<sup>18–20</sup> In this review, we summarise previous reports using electrochemical approaches to study the electronic structures of  $\text{Au}_n(\text{SR})_m$  NCs. In section 2, we provide a brief history of synthesis of  $\text{Au}_n(\text{SR})_m$  NCs. In section 3, we discuss the principles of electrochemical measurement techniques and provide reported examples of the electronic structures of  $\text{Au}_n(\text{SR})_m$  NCs determined by electrochemical methods. In section 4, we summarise previous work and discuss the future outlook of this field. Studies on electrochemical catalysis<sup>21–24</sup> and synthesis of Au NCs<sup>9,25–27</sup> were excluded from the present review because they have been described in detail elsewhere.

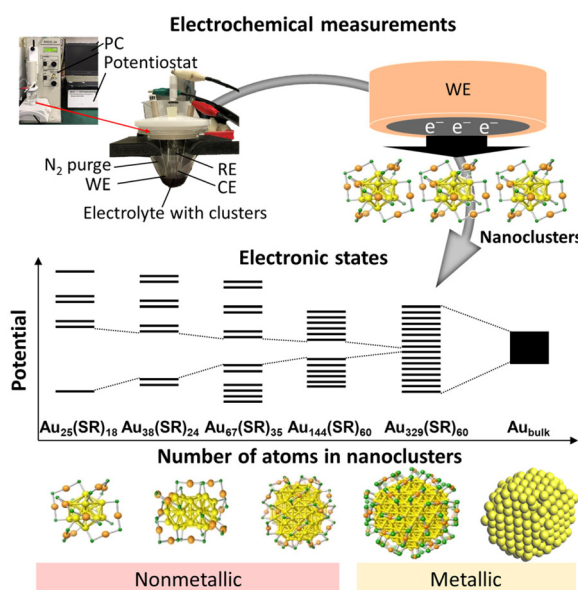


Fig. 1 Schematic of electrochemical measurements for elucidation of the electronic structure of metal clusters.

## 2 Thiolate-protected gold nanoclusters

The characteristics of the electronic structures of metal NCs are between those of metal complexes and metal NPs. Consequently, they have many similarities in their synthetic methods. As in general synthesis of metal NPs, metal NCs are obtained by mixing a solution containing organic ligands with metal salts as precursors with addition of a reducing agent. Such liquid-phase synthesis is called a bottom-up method. Since the late 1960s, efforts have been made to synthesise metal NCs consisting of Au, platinum (Pt), and palladium (Pd) with phosphine, halogen (X), and carbon monoxide (CO) as ligands.<sup>28–32</sup> Moreover, metal NCs comprising SR-protected Au, silver (Ag), copper (Cu), Pt, and Pd have also been reported.  $\text{Au}_n(\text{SR})_m$  NCs are extremely stable in air owing to the strong bonding between Au and sulfur (S).<sup>33,34</sup> Therefore, precise separation and synthesis of a single chemical composition of these  $\text{Au}_n(\text{SR})_m$  NCs was attempted relatively early.<sup>35,36</sup> In general,  $\text{Au}_n(\text{SR})_m$  NCs are synthesised by (i) adding a metal salt (e.g., gold chloride) to a solvent, (ii) adding a thiol as a ligand, and (iii) mixing with a reducing agent (e.g., sodium borohydride). The by-products and remaining SR complex are then washed off with solvent to obtain  $\text{Au}_n(\text{SR})_m$  NCs with a uniform number of constituent atoms. In addition to SR, a number of syntheses using phosphine, *N*-heterocyclic carbene, and alkynyl ligands have also been reported.<sup>37,38</sup> Moreover, some Au atoms in  $\text{Au}_n(\text{SR})_m$  NCs can be exchanged by Ag, Cu, Pt, Pd, iridium (Ir), mercury (Hg), cadmium (Cd) and so on. For  $\text{Au}_n(\text{SR})_m$  NCs, many of their geometric structures have been determined by SCXRD.<sup>39</sup> In conjunction with the development of these synthetic methods, the resulting  $\text{Au}_n(\text{SR})_m$  NCs has been used as luminescent materials,<sup>40–42</sup> chemical sensors,<sup>43</sup> photosensitisers,<sup>44–46</sup> catalysts,<sup>11,47–49</sup> electrocatalysts,<sup>22,49–53</sup> and photocatalysts.<sup>49,54,55</sup> This is because the unique electronic/geometric structures of  $\text{Au}_n(\text{SR})_m$  NCs give rise to properties and functions that are not observed in bulk metals and metal NPs. Research on metal NCs, which can be regarded as ultimate nanomaterials based on atomically precise control, has become increasingly active in recent years.

## 3 Electronic structures of thiolate-protected metal nanoclusters by electrochemical methods

In this section, we describe the basic experimental techniques of electrochemical measurements and describe a series of studies on the electronic structures of  $\text{Au}_n(\text{SR})_m$  NCs among the studies of metal NCs using electrochemical measurement techniques.

### 3.1 Electrochemical methods for determination of the electronic structures of metal nanoclusters

There are two main parameters used in electrochemical measurements: the voltage (potential) and the current. The

potential is the energy applied to the electrodes to cause a reaction (Fig. 2a), while the current indicates the reaction rate. By controlling these parameters, the causal relationship between them and their correlation with time can be investigated. In basic electrochemical measurements, three-electrode (working electrode (WE), reference electrode (RE), and counter electrode (CE)) or two-electrode (WE and CE) systems are used. The WE is the main electrode in the electrochemical reaction, and electrons are transferred and chemical reactions occur on its surface. The RE is used to control the potential of the WE and as a standard of the potential for the measurements. The CE is paired with the WE and serves to conduct unwanted current. These electrodes are immersed in an electrolyte containing the reactants, and the potential and current are controlled using a potentiostat to make electrochemical measurements. They can also be evaluated as a solid device by using a solid electrolyte instead of a solution electrolyte. Electrochemical measurement methods can be divided into several measurement methods depending on the settings of the potential and current (Fig. 2).

Among the electrochemical measurement methods, voltammetry is the most basic method for measuring the flowing current by continuously changing the potential of the WE. Linear sweep voltammetry (LSV) is a technique in which the potential is swept in one direction and the current is measured (Fig. 2b). The measurement method in which the potential is folded back and the applied potential cycle is swept repeatedly

in a specific potential range is called cyclic voltammetry (CV) (Fig. 2c). CV is widely used as a general purpose method because it provides a rough state of the electrochemical condition on the surface of the WE. Furthermore, it can provide information about (i) the ease of oxidation or reduction of the reactants dissolved in the electrolyte, (ii) the chemical reactions at the surface of the WE, and (iii) the species adsorbed on the surface of the WE. The direction and rate of sweep of the applied potential are important parameters, and their behaviour depends on the reversibility of the electrochemical reactions.

LSV and CV gradually change the applied voltage over a period of time and monitor the current during that time. In contrast, pulse voltammetry applies pulse-stepped potentials and measures the current. In LSV and CV, the reaction proceeds with the charging of the electrical double layer at the surface of the electrode, because the potential gradually changes with time. This makes it difficult to separate the non-faradaic current (*i.e.*, the capacitive current) from the faradaic current (*i.e.*, the reaction current). However, in pulse voltammetry, the charging of the electric double layer immediately ends after the applied potential step, so that the faradaic current can be separated and extracted. Therefore, by giving a slightly different potential each time and plotting the current values at regular intervals, more detailed analysis can be performed using pulse voltammetry compared with LSV and CV. Depending on the shape of the pulse, the measurements can be classified as normal pulse voltammetry (NPV, Fig. 2d), differential pulse voltammetry (DPV, Fig. 2e), and square-wave voltammetry (SWV, Fig. 2f). SWV can significantly reduce the measurement time compared with normal pulse voltammetry and DPV because the step potential is gradually increased. In recent years, pulse voltammetry has been used to determine the electronic states of metal NCs, and it can be combined with optical absorption spectroscopy, luminescence measurements, and DFT calculations to investigate the electronic structures of metal NCs in detail.

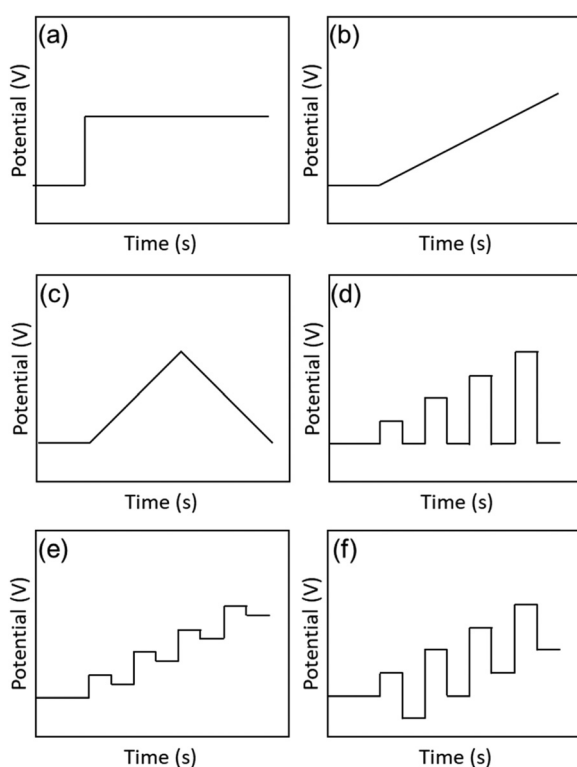


Fig. 2 Electrochemical methods: (a) chronoamperometry, (b) LSV, (c) CV, (d) NPV, (e) DPV, and (f) SWV.

### 3.2 Determination of the electronic structures of metal nanoclusters

The earliest study of voltammetry of small metal NPs was reported by Mulvaney and co-workers in 1997.<sup>19,56</sup> Initially, single-electron tunnelling microelectrode measurements using scanning tunnelling microscopy was the main focus.<sup>57,58</sup> In 1998, Whetten and co-workers<sup>59</sup> performed electrochemical analysis of  $\text{Au}_n(\text{SR})_m$  NCs, which were easily obtained by liquid-phase synthesis (Fig. 3). The electronic structures of  $\text{Au}_n(\text{SR})_m$  NCs with sizes of 8–38 kDa (1.1–1.9 nm in diameter) protected with an alkanethiolate (butanethiolate ( $\text{SC}_4\text{H}_9$ ) or hexanethiolate ( $\text{SC}_6\text{H}_{13}$ ))) were evaluated by DPV measurement.

The double-layer capacitance of small NCs can be modelled by considering the NC to be a concentric sphere capacitor. The inner and outer spheres have different radii, which correspond to the metal-core radius ( $r$ ) and the thickness of the SR ligand layer ( $d$ ) in  $\text{Au}_n(\text{SR})_m$ , respectively. Considering the dielectric



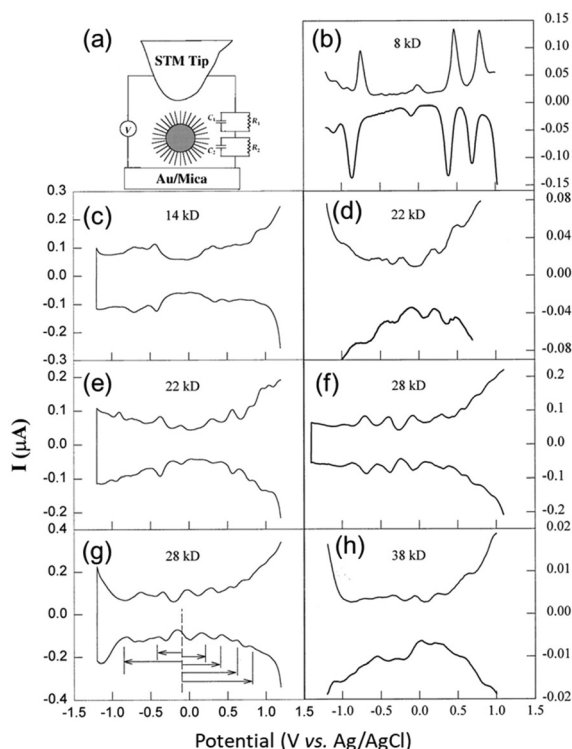


**Fig. 3** (a) Schematic of the scanning tunnelling microscopy double tunnel-junction model. Differential pulse voltammograms of (b), (d), (f) and (h) hexanethiolate-, and (c), (e), and (g) butanethiolate-Au NCs as a function of the uniform core size in 0.05 M tetrabutylammonium perchlorate/toluene/acetonitrile (2 : 1 = v : v) at a  $9.5 \times 10^{-3} \text{ cm}^2$  Pt electrode (direct current potential scan at  $10 \text{ mV s}^{-1}$  with a pulse amplitude of 50 mV). The sizes and concentrations were (b) 8 kDa and 0.30 mM, (c) 14 kDa and 0.086 mM, (d) 22 kDa and 0.10 mM, (e) 22 kDa and 0.032 mM, (f) 28 kDa and 0.10 mM, (g) 28 kDa and 0.10 mM, and (h) 38 kDa and 0.10 mM. Reproduced with permission from ref. 59. Copyright 1998, AAAS.

function of the SR ligand layer, the capacitance of the NC ( $C_{\text{NC}}$ ) is described by the following eqn (1):<sup>60,61</sup>

$$C_{\text{NC}} = 4\pi\epsilon\epsilon_0 \frac{r}{d} (r + d) \quad (1)$$

where  $\epsilon$  is the effective dielectric constant of the SR layer and  $\epsilon_0$  is the permittivity of free space.

Assuming that  $C_{\text{NC}}$  does not vary with the charge of the metal core, a continuous series of charge steps ( $\Delta V_c$ ) occurs at regular intervals when the metal core catches and releases one electron:

$$V_c = \frac{e}{C_{\text{NC}}} \quad (2)$$

where  $\Delta V_c$  is the critical voltage bias,  $C_{\text{NC}}$  is the capacitance, and  $e$  is the electron charge. Such constant-interval charging steps are actually observed in these  $\text{Au}_n(\text{SR})_m$  NCs.  $C_{\text{NC}}$  exhibits a minimum value close to the zero-charge potential of the charged interface.  $\text{Au}_n(\text{SR})_m$  NCs also exhibit similar double-layer capacitance regardless of whether they are dissolved in solution or deposited on a surface.<sup>62</sup>

Based on eqn (2), the large  $\text{Au}_n(\text{SR})_m$  NCs (22–38 kDa) exhibited a Coulomb staircase-like response consistent with a metallic double-layer charge (Fig. 3e and f). In contrast, the small  $\text{Au}_n(\text{SR})_m$  NCs (8 and 14 kDa) exhibited trends like a molecule (Fig. 3b and c), including a large central gap (1.2 and 0.7 V vs. Ag/AgCl for the 8 kDa  $\text{Au}_n(\text{SR})_m$  NCs). Such molecule-like behaviour of the small  $\text{Au}_n(\text{SR})_m$  NCs is similar to that of Pt carbonyl NCs,<sup>63</sup> and it is consistent with the highest occupied molecular orbital (HOMO)–lowest unoccupied molecular orbital (LUMO) gaps obtained from the optical absorption spectra.

Studies then started to estimate the HOMO–LUMO (H–L) gaps of  $\text{Au}_n(\text{SR})_m$  NCs by electrochemical methods, such as DPV.<sup>60,62,64–70</sup> However, the electronic structures of  $\text{Au}_n(\text{SR})_m$  NCs controlled with atomic precision were only revealed electrochemically from 2004. The development of methods for synthesis and isolation of  $\text{Au}_n(\text{SR})_m$  NCs and establishment of evaluation methods, such as the development of mass spectrometry instruments, significantly contributed to this breakthrough. In recent years, the electronic structures of a number of Au NCs have been clarified. Such information about the electronic structure can also be obtained by optical absorption spectroscopy and DFT calculations. The H–L gaps of  $\text{Au}_n(\text{SR})_m$  NCs determined by electrochemical methods are summarised in Table 1, along with information<sup>71,72</sup> about the electronic structures obtained by other methods. In this review, the effects of the representative factors of the (i) size, (ii) ligand, (iii) introduction of other elements, and (iv) geometrical structure changes on the electronic structures of  $\text{Au}_n(\text{SR})_m$  NCs are introduced.

### 3.3 Size effect on the electronic structure of thiolate-protected gold nanoclusters

In 2004, Murray and co-workers<sup>73</sup> found that the electrochemically determined band gap of  $\text{Au}_{38}(\text{PET})_{24}$  (PET = 2-phenylethylthiolate), which was later modified to  $\text{Au}_{25}(\text{PET})_{18}$  (Fig. 4A) owing to developments in mass spectrometry, was consistent with the optically determined band gap.<sup>74</sup>  $\text{Au}_{25}(\text{PET})_{18}$  was dissolved in a mixture of toluene/acetonitrile or dichloromethane ( $\text{CH}_2\text{Cl}_2$ ) containing 0.1 M tetrabutylammonium hexafluorophosphate (TBAPF<sub>6</sub>) using 0.4 mm-diameter Pt for the WE, a Ag wire for the pseudo-RE (Ag QRE), and a Pt wire for the CE. The dissolved  $\text{Au}_{25}(\text{PET})_{18}$  was evaluated by DPV and CV (Fig. 4B). A resting potential of  $-0.1 \text{ V}$  vs. Ag QRE was observed at  $25 \text{ }^\circ\text{C}$ , with the first one-electron oxidation peak (O1) slightly on the positive side. Conversely, the first one-electron reduction peak (R1) was largely on the negative side, showing a large energy gap (1.62 V) (Fig. 4B and C). The potential intervals were calculated to be 0.73, 0.29, and 1.62 V for the O3–O2, O2–O1, and O1–R1 transitions, respectively. In this case, measurements at low temperature ( $-70 \text{ }^\circ\text{C}$ ) contributed to the reversibility, especially in the high oxidation state. In general, the energy gap between the initial one-electron oxidation and one-electron reduction (O1–R1) is the H–L gap including the electron and hole charging energies. Therefore, to calculate the pseudo-H–L gap, this charging energy has to be subtracted.

**Table 1** Experimental and theoretical HOMO–LUMO gaps ( $E_g$ ) of the thiolate-protected Au NCs mentioned in this review

Composition	Geometric structure	Conditions for the electrochemical measurements	$E_g^e$ [eV] <sup>a</sup>	$E_g^o$ [eV] <sup>b</sup>	$E_g^c$ [eV] <sup>c</sup>	Ref. <sup>d</sup>
$\text{Au}_{18}(\text{SC}_6\text{H}_{11})_{14}$	$\text{Bi-O}_h^e$	RT, DPV, 0.1 M TBAPF <sub>6</sub> /CH <sub>2</sub> Cl <sub>2</sub> <sup>f</sup>	1.91	1.7	—	75
$\text{Au}_{15}\text{Ag}_3(\text{SC}_6\text{H}_{11})_{14}$		RT, DPV, 0.1 M TBAPF <sub>6</sub> /CH <sub>2</sub> Cl <sub>2</sub>	2.11	2.0	—	75
$[\text{Au}_{25}(\text{SC}_6\text{H}_5)_{18}]^-$	$I_h^h$	RT, DPV, 0.1 M TBAPF <sub>6</sub> /CH <sub>2</sub> Cl <sub>2</sub>	1.16	—	—	113
$[\text{Au}_{25}(\text{SC}_6\text{H}_{13})_{18}]^-$		RT, SWV, 0.1 M TBAPF <sub>6</sub> /CH <sub>2</sub> Cl <sub>2</sub>	1.32	1.3	—	88
		RT, DPV, 0.1 M TBAPF <sub>6</sub> /CH <sub>2</sub> Cl <sub>2</sub> : toluene	~1.65	—	—	108
		RT, DPV, 0.1 M TBAPF <sub>6</sub> /CH <sub>2</sub> Cl <sub>2</sub>	1.25	—	—	113
		SWV, 0.1 M TBAPF <sub>6</sub> /CH <sub>2</sub> Cl <sub>2</sub>	1.31	—	—	89
$\text{Au}_{25}(\text{SC}_n\text{H}_{2n+1})_{18}$ ( $n = 2-12$ )		RT, DPV, 0.1 M TBAPF <sub>6</sub> /CH <sub>2</sub> Cl <sub>2</sub>	1.29–1.31	—	—	99
$[\text{Au}_{25}(\text{MPS})_{18}]^g$		RT, DPV, 0.1 M TBAPF <sub>6</sub> /CH <sub>2</sub> Cl <sub>2</sub> : toluene	1.39–1.66	—	—	108
$[\text{Au}_{25}(\text{PET})_{18}]^-$		RT, DPV, 0.1 M TBAPF <sub>6</sub> /CH <sub>2</sub> Cl <sub>2</sub>	1.34	—	—	76
		RT, DPV, 0.1 M TBAPF <sub>6</sub> /DMF	1.44	—	—	76
		RT, DPV, 0.1 M TBAPF <sub>6</sub> /CH <sub>2</sub> Cl <sub>2</sub>	1.23	—	—	113
		273 K, DPV, 0.1 M TBAPF <sub>6</sub> /CH <sub>2</sub> Cl <sub>2</sub>	1.30	1.17	—	116
		DPV, 0.1 M TBAP/acetone: acetonitrile <sup>i</sup>	1.54	—	—	80
		RT, DPV, 0.1 M TBAPF <sub>6</sub> /CH <sub>2</sub> Cl <sub>2</sub>	0.38	—	—	112
		SWV, 0.1 M TBAPF <sub>6</sub> /CH <sub>2</sub> Cl <sub>2</sub>	0.34	—	—	110
			0.32	—	—	110
		RT, DPV, 0.1 M TBAPF <sub>6</sub> /CH <sub>2</sub> Cl <sub>2</sub>	1.20	—	—	113
			1.29	—	—	112
			1.28	—	—	
			1.41	1.37	—	
			1.46	1.41	—	
		273 K, DPV, 0.1 M TBAPF <sub>6</sub> /CH <sub>2</sub> Cl <sub>2</sub>	1.29	1.22	—	116
			>1.80	1.40	—	
			1.45	1.41	—	
		RT, DPV, 0.1 M TBAPF <sub>6</sub> /CH <sub>2</sub> Cl <sub>2</sub>	1.54	1.82	—	101
		DPV, TBAPF <sub>6</sub> /CH <sub>2</sub> Cl <sub>2</sub>	1.57	~1.4	—	119
			1.29	~1.2	—	
		RT, DPV, 0.5 M BTPPATBF <sub>20</sub> /CH <sub>2</sub> Cl <sub>2</sub> <sup>l</sup>	1.96	1.71	1.51–1.79	81
		RT, DPV, 0.1 M TBAPF <sub>6</sub> /CH <sub>2</sub> Cl <sub>2</sub>	0.77	0.83	—	82
		RT, DPV, 0.1 M TBAPF <sub>6</sub> /CH <sub>2</sub> Cl <sub>2</sub>	1.00	0.92	—	83
		RT, SWV, 0.1 M TBAPF <sub>6</sub> /CH <sub>2</sub> Cl <sub>2</sub>	0.99	0.9	—	88
		SWV, 0.1 M TBAPF <sub>6</sub> /CH <sub>2</sub> Cl <sub>2</sub>	0.86	—	1.01	114
		SWV, 0.1 M TBAPF <sub>6</sub> /CH <sub>2</sub> Cl <sub>2</sub>	0.26	—	0.23	114
		SWV, 0.1 M TBAPF <sub>6</sub> /CH <sub>2</sub> Cl <sub>2</sub>	0.95	—	1.10	114
		RT, DPV, 0.5 M TBAPF <sub>6</sub> /THF	0.74	—	0.75	84
		RT, SWV, 0.1 M TBAPF <sub>6</sub> /CH <sub>2</sub> Cl <sub>2</sub>	0.61	0.7	—	88
		RT, SWV, 0.1 M TBAPF <sub>6</sub> /CH <sub>2</sub> Cl <sub>2</sub>	0.18	<0.5	—	88
		RT, DPV, 0.1 M TBAPF <sub>6</sub> /CH <sub>2</sub> Cl <sub>2</sub>	0.38	0.42	—	105
		RT, DPV, BTPPATBF <sub>20</sub> /CH <sub>2</sub> Cl <sub>2</sub>	0.21	—	—	85
		RT, SWV, 0.1 M TBAPF <sub>6</sub> /CH <sub>2</sub> Cl <sub>2</sub>	0.15	<0.5	—	88
		RT, SWV, 0.1 M TBAPF <sub>6</sub> /CH <sub>2</sub> Cl <sub>2</sub>	0.04	<0.5	—	88

<sup>a</sup> Electrochemical HOMO–LUMO gap. <sup>b</sup> Optical HOMO–LUMO gap. <sup>c</sup> DFT-calculated HOMO–LUMO gap. <sup>d</sup> Reference number. <sup>e</sup> Bi- $O_h$ : Bi-octahedral. <sup>f</sup> TBAPF<sub>6</sub>: tetrabutylammonium hexafluorophosphate. <sup>g</sup> MPS: (3-mercaptopropyl)sulfonate. <sup>h</sup>  $I_h$ : icosahedral. <sup>i</sup> BAP: tetra-*n*-butylammonium perchlorate. <sup>j</sup> Bi- $I_h$ : bi-icosahedral. <sup>k</sup> FCC: face-centered cubic. <sup>l</sup> BTPPATBF<sub>20</sub>: bis(triphenyl phosphoranylidene)ammonium tetrakis(pentafluorophenyl). <sup>m</sup> Tri- $I_h$ : tri-icosahedral. <sup>n</sup> S-Nap: 2-naphthalenethiolate. <sup>o</sup>  $D_h$ : decahedral. Room temperature (RT).

The charging energy was estimated to be 0.29 V, which corresponded to the O2–O1 transition. Because the energy gap between the initial one-electron oxidation and one-electron reduction in CH<sub>2</sub>Cl<sub>2</sub> was 1.62 V (O1–R1), a value of 1.33 eV was obtained by subtracting the charging energy of 0.29 V (O2–O1). The absorption edge wavelength (*i.e.*, the H–L gap) obtained from the optical absorption spectrum was 1.33 eV, which was in close agreement with the electrochemically determined H–L gap (Fig. 4C). Subsequently, several groups reported the H–L gaps of  $\text{Au}_{18}(\text{SC}_6\text{H}_{11})_{14}$ ,<sup>75</sup>  $[\text{Au}_{25}(\text{SR})_{18}]^-$ ,<sup>76–80</sup>  $\text{Au}_{36}(\text{SPh})_{24}$  (SPh = benzenethiolate),<sup>81</sup>  $[\text{Au}_{37}(\text{PPh}_3)_{10}(\text{PET})_{10}\text{Cl}_2]^+$  (PPh<sub>3</sub> = triphenylphosphine),<sup>82</sup>  $\text{Au}_{38}(\text{SR})_{24}$ ,<sup>68,83</sup>  $\text{Au}_{67}(\text{PET})_{35}$ ,<sup>84</sup>  $\text{Au}_{130}(\text{PET})_{50}$ ,<sup>85</sup>  $\text{Au}_{130}(\text{Dur-DT})_{29}(\text{PET})_{22}$  (Dur-DT = durene-dithiolate),<sup>86</sup> and  $\text{Au}_{133}(\text{TBBT})_{52}$  (TBBT = *tert*-butylbenzenethiolate),<sup>87</sup> which were estimated by electrochemical measurements.

Lee and co-workers<sup>88,89</sup> used  $\text{Au}_{25}(\text{SC}_6\text{H}_{13})_{18}$ ,  $\text{Au}_{38}(\text{SC}_6\text{H}_{13})_{24}$ ,  $\text{Au}_{67}(\text{SC}_6\text{H}_{13})_{35}$ ,  $\text{Au}_{102}(\text{SC}_6\text{H}_{13})_{44}$ ,  $\text{Au}_{144}(\text{SC}_6\text{H}_{13})_{60}$ , and  $\text{Au}_{333}(\text{SC}_6\text{H}_{13})_{79}$  to obtain the size effect of the H–L gap. They performed SWV measurements of each  $\text{Au}_n(\text{SR})_m$  NC (Fig. 5A). The electrochemical H–L gaps were determined to be 1.32, 0.99, 0.61, 0.18, and 0.15 eV for  $\text{Au}_{25}(\text{SC}_6\text{H}_{13})_{18}$ ,  $\text{Au}_{38}(\text{SC}_6\text{H}_{13})_{24}$ ,  $\text{Au}_{67}(\text{SC}_6\text{H}_{13})_{35}$ ,  $\text{Au}_{102}(\text{SC}_6\text{H}_{13})_{44}$ , and  $\text{Au}_{144}(\text{SC}_6\text{H}_{13})_{60}$ , respectively (Fig. 5B). A significantly size-dependent O1–R1 gap was observed for the small  $\text{Au}_n(\text{SR})_m$  NCs. The O1–R1 gaps of  $\text{Au}_{102}(\text{SC}_6\text{H}_{13})_{44}$ ,  $\text{Au}_{144}(\text{SC}_6\text{H}_{13})_{60}$ , and  $\text{Au}_{333}(\text{SC}_6\text{H}_{13})_{79}$  were considerably smaller than those of the relatively small  $\text{Au}_n(\text{SR})_m$  NCs (0.49, 0.39 and 0.22 V, respectively), and the O1 and R1 peaks were observed with equally spaced current peaks along with other peaks. This suggests that  $\text{Au}_{102}(\text{SC}_6\text{H}_{13})_{44}$ ,  $\text{Au}_{144}(\text{SC}_6\text{H}_{13})_{60}$ , and  $\text{Au}_{333}(\text{SC}_6\text{H}_{13})_{79}$  work as quantum capaci-



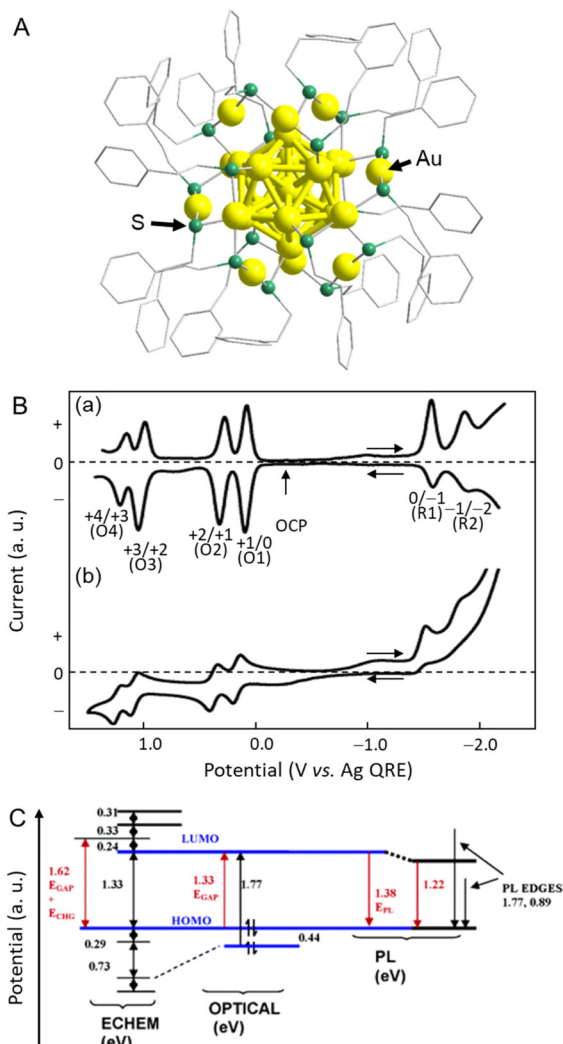


**Fig. 4** (A) Geometric structure of  $[Au_{25}(PET)_{18}]^-$ . (B) (a)  $25\text{ }^\circ\text{C}$  DPVs at  $0.02\text{ V s}^{-1}$ , and (b)  $-70\text{ }^\circ\text{C}$  cyclic voltammogram ( $0.1\text{ V s}^{-1}$ ) of  $Au_{25}(PET)_{18}$  in  $0.1\text{ M}$  TBAPF<sub>6</sub> in degassed  $CH_2Cl_2$  with a  $0.4\text{ mm}$ -diameter Pt WE, a Ag-wire quasi-RE, and a Pt-wire CE. The arrows indicate the solution rest potentials, and \* indicates the wave for incompletely removed  $O_2$ , which varied from experiment to experiment. (C) Energy level diagram for  $Au_{25}(PET)_{18}$  based on the data in  $CH_2Cl_2$  solution. Reproduced with permission from ref. 74. Copyright 2004, American Chemical Society.

tors that exhibit the charging characteristics of a quantum double layer. In other words, the double-layer capacitance of these  $Au_n(SR)_m$  NCs is sufficiently small that the potential spacing between successive single-electron changes of the charge on the NC core becomes experimentally observable. The optical absorption spectra of  $Au_{25}(SC_6H_{13})_{18}$ ,  $Au_{38}(SC_6H_{13})_{24}$ , and  $Au_{67}(SC_6H_{13})_{35}$  showed absorption edges of 1.3, 0.9, and 0.7 eV, respectively. The absorption edges corresponded to the  $Au_n(SR)_m$  optical gaps for the electronic transitions, and the absorption edge decreased with increasing  $Au_n(SR)_m$  size. For relatively large  $Au_n(SR)_m$  NCs, such as  $Au_{102}(SC_6H_{13})_{44}$ ,  $Au_{144}(SC_6H_{13})_{60}$ , and  $Au_{333}(SC_6H_{13})_{79}$ , the optical energy gap

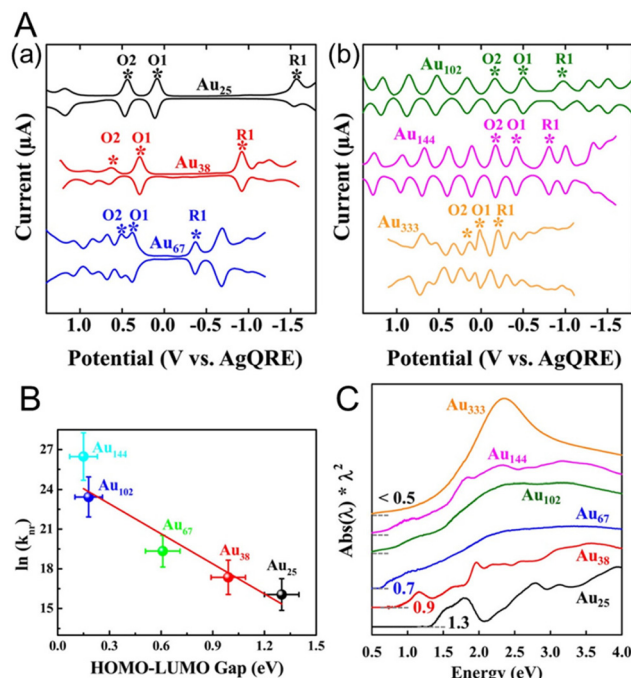


**Fig. 5** (A) Square-wave voltammograms of (a)  $Au_{25}(SC_6H_{13})_{18}$ ,  $Au_{38}(SC_6H_{13})_{24}$ , and  $Au_{67}(SC_6H_{13})_{35}$  and (b)  $Au_{102}(SC_6H_{13})_{44}$ ,  $Au_{144}(SC_6H_{13})_{60}$ , and  $Au_{333}(SC_6H_{13})_{79}$  in  $CH_2Cl_2$  containing  $0.1\text{ M}$  TBAPF<sub>6</sub>. (B) Plot of  $\ln(k_{nr})$  versus the H-L gap for gold clusters. The solid line is the best fit straight line for the data ( $Au_{25}$ – $Au_{144}$ ). (C) Ultraviolet–visible–near-infrared absorption spectra of  $Au_{25}(SC_6H_{13})_{18}$ ,  $Au_{38}(SC_6H_{13})_{24}$ ,  $Au_{67}(SC_6H_{13})_{35}$ ,  $Au_{102}(SC_6H_{13})_{44}$ ,  $Au_{144}(SC_6H_{13})_{60}$ , and  $Au_{333}(SC_6H_{13})_{79}$ . Reproduced with permission from ref. 88. Copyright 2017, American Chemical Society.

was less than  $0.5\text{ eV}$  and the absorption edge became less distinct. In this respect, the electrochemical method was able to calculate the H-L gap with higher accuracy than optical absorption spectroscopy. From the optical absorption spectrum,  $Au_{333}(SC_6H_{13})_{79}$  showed a prominent band of surface plasmon resonance at approximately  $2.3\text{ eV}$ . This indicates that electrons collectively oscillate within  $Au_{333}(SC_6H_{13})_{79}$  in response to the incident optical electric field, indicating that it has metallic properties.

The electronic structure of  $Au_{329}(PET)_{84}$ , a relatively large  $Au_n(SR)_m$  NC, was further analysed electrochemically by Dass and co-workers.<sup>90</sup> They found that over a potential window of approximately  $4\text{ V}$ ,  $Au_{329}(PET)_{84}$  exhibited 22 electronic states. In this study, the capacitance varied in proportion to the size of the  $Au_n(SR)_m$  NC. The transition of the electronic state from molecular to metallic in  $Au_n(SR)_m$  is still not completely understood.  $Au_{246}(p\text{-MBT})_{80}$  ( $p\text{-MBT} = p\text{-methylbenzenethiolate}$ ) is the largest non-metallic  $Au_n(SR)_m$  NC and  $Au_{279}(TBBT)_{84}$  is the smallest metallic  $Au_n(SR)_m$  NC, as revealed by Jin and co-workers<sup>91–94</sup> by transient absorption spectroscopy. However, while  $Au_{246}(p\text{-MBT})_{80}$  has an octahedral structure,  $Au_{279}(TBBT)_{84}$  has a face-centred cubic (fcc) structure. The influences of the differences in the geometry and ligand effect

have not been clarified, so further investigation is required.<sup>95,96</sup>

The small size region of  $\text{Au}_n(\text{SR})_m$  NCs was further investigated by Jin and co-workers<sup>97</sup> using  $\text{Au}_{133}(\text{TBBT})_{52}$  and  $\text{Au}_{144}(\text{BM})_{60}$  ( $\text{BM}$  = phenylmethanethiolate). They found that the charging energy decreases with the catch and release of  $\text{Au}_n(\text{SR})_m$  electrons in the more oxidised/reduced state (Fig. 6). This trend can be attributed to an increase in the capacitance of  $\text{Au}_n(\text{SR})_m$  due to an increase in the dielectric constant of the ligand monolayer by penetration or intercalation of electrolyte ions. Indeed, when the temperature during the electrochemical measurements of  $\text{Au}_{133}(\text{TBBT})_{52}$  was lowered to 195 K, the charging energy became independent of the redox state and showed a constant value (Fig. 6A and B). Interestingly, the charging energy was much less sensitive to temperature changes for  $\text{Au}_{133}(\text{TBBT})_{52}$  in the reduced state compared with oxidised  $\text{Au}_{133}(\text{TBBT})_{52}$ . To access the core stabilised by the bulky *tert*-butyl terminal functional group, the tetrabutylammonium cation is considerably less accessible than the perchloride anion because of steric hindrance. The relatively large decrease in the charging energy of oxidised NCs in the low temperature measurements could be due to suppression of the movement of such sterically hindered molecules at low temperature. Conversely, the BM monolayer of  $\text{Au}_{144}(\text{BM})_{60}$  is more flexible owing to the absence of the bulky *tert*-butyl group between the S atom and the phenyl group. Therefore,  $\text{Au}_{144}(\text{BM})_{60}$  exhibits a smaller peak potential spacing owing to it having larger capacitance than  $\text{Au}_{133}(\text{TBBT})_{52}$  with roughly the same sized metal core (Fig. 6C and D).

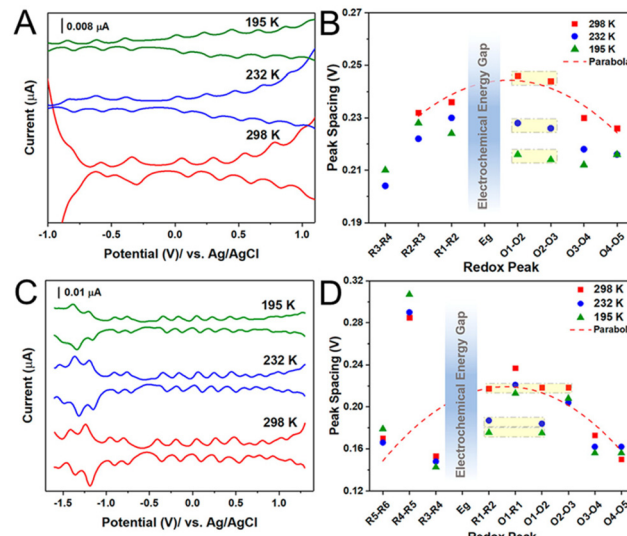


**Fig. 6** Temperature dependence of electrochemical properties of  $\text{Au}_{133}(\text{TBBT})_{52}$  and  $\text{Au}_{144}(\text{BM})_{60}$ . (A and C) The DPVs and (B and D) the electrochemical peak spacing of (A and B)  $\text{Au}_{133}(\text{TBBT})_{52}$  and (C and D)  $\text{Au}_{144}(\text{BM})_{60}$  at 298, 232, and 195 K. Peak spacing  $\Delta V$ s in (B) and (C) analyzed from (A) and (C), respectively. Reproduced with permission from ref. 97. Copyright 2020, American Chemical Society.

### 3.4 Ligand effect on the electronic structure of thiolate-protected gold nanoclusters

Changes in the ligand from the S atom onwards have little effect on the electrochemically determined H-L gap in many cases,<sup>74,90,97–101</sup> but replacing the S atom with a different element causes a change in the H-L gap.

Negishi and co-workers<sup>102</sup> investigated the ligand dependence using  $[\text{Au}_{25}(\text{PET})_{18-x}(\text{SePh})_x]^-$  ( $\text{SePh}$  = benzeneselenolate) and  $[\text{Au}_{25}(\text{PET})_{18-x}(\text{TePh})_x]^-$  ( $\text{TePh}$  = benzenetellurolate) by DPV measurements in 2016 (Fig. 7A). When the PET ligands were replaced by SePh or TePh, the redox potentials of R1 and O1 shifted towards the positive side (Fig. 7B). However, when the PET ligands were replaced by SePh, the redox potentials of O2 and O3 shifted to the negative side in the final step of ligand exchange (around  $x = 18$ ) (Fig. 7B). Furthermore, the H-L gap narrowed as the number of exchanges increased. The relationships between the changes in the redox potentials of O2 and O3 and the number of exchanged ligands were not linear. This is presumably because of changes in the framework structure of the NC with increasing number of exchanged ligands, reflecting the difference in the atomic radii of S and Se. A similar trend was also reported by Zhu and co-workers<sup>103</sup> using  $[\text{Au}_{25}(\text{PET})_{18}]^-$  and  $[\text{Au}_{25}(\text{SePh})_{18}]^-$ .

In 2019, Tsukuda and co-workers<sup>104</sup> reported the electronic structures of C≡CR-protected Au NCs by electrochemical measurements. The electrochemically determined superatomic orbital 1P–1D gaps of  $[\text{Au}_{25}(\text{PET})_{18}]^-$  and  $[\text{Au}_{25}(\text{C}≡\text{CAr}^F)_{18}]^-$

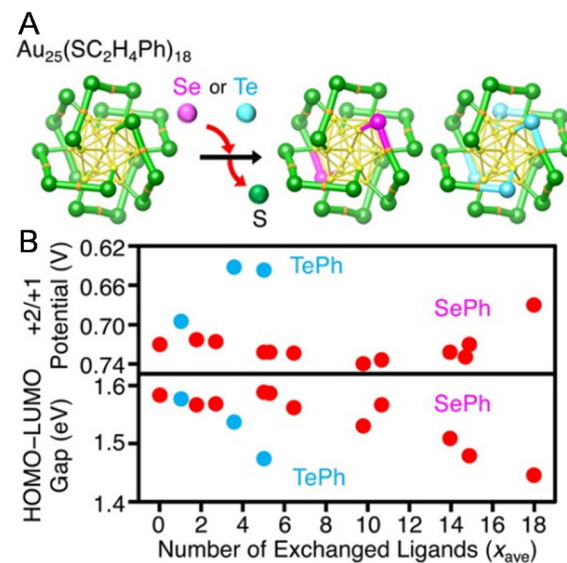


**Fig. 7** (A) Framework structures of  $[\text{Au}_{25}(\text{PET})_{18-x}(\text{SePh})_x]^-$  and  $[\text{Au}_{25}(\text{PET})_{18-x}(\text{TePh})_x]^-$  determined by SCXRD. (B) Relationships of the peak energy of O3 and the H-L gap with the average number of exchanged ligands ( $x_{\text{ave}}$ ) for  $[\text{Au}_{25}(\text{PET})_{18}]^-$ ,  $[\text{Au}_{25}(\text{PET})_{18-x}(\text{SePh})_x]^-$ , and  $[\text{Au}_{25}(\text{PET})_{18-x}(\text{TePh})_x]^-$ . In the experiments, each cluster was dissolved in 0.1 M tetrabutylammonium perchlorate in  $\text{CH}_2\text{Cl}_2$ . DPV was performed at room temperature. Reproduced with permission from ref. 102. Copyright 2016, American Chemical Society.



( $\text{Ar}^{\text{F}} = 3,5-(\text{CF}_3)_2\text{C}_6\text{H}_3$ ) were 1.93 and 1.8 eV, respectively (Fig. 8A). A similar trend was observed when the superatomic orbital 1P–1D gaps were determined from the optical absorption spectra, with  $[\text{Au}_{25}(\text{C}\equiv\text{CAr}^{\text{F}})_{18}]^-$  having a smaller 1P–1D gap than  $[\text{Au}_{25}(\text{PET})_{18}]^-$  (Fig. 8B). This can be attributed to the stronger cationic nature of Au in  $[\text{Au}_{25}(\text{C}\equiv\text{CAr}^{\text{F}})_{18}]^-$  than in  $[\text{Au}_{25}(\text{PET})_{18}]^-$ . The ligand dependence on the H–L gap owing to the change of the Au–S interface has been reported to be limited to relatively small  $\text{Au}_n(\text{SR})_m$  NCs.<sup>105–107</sup>

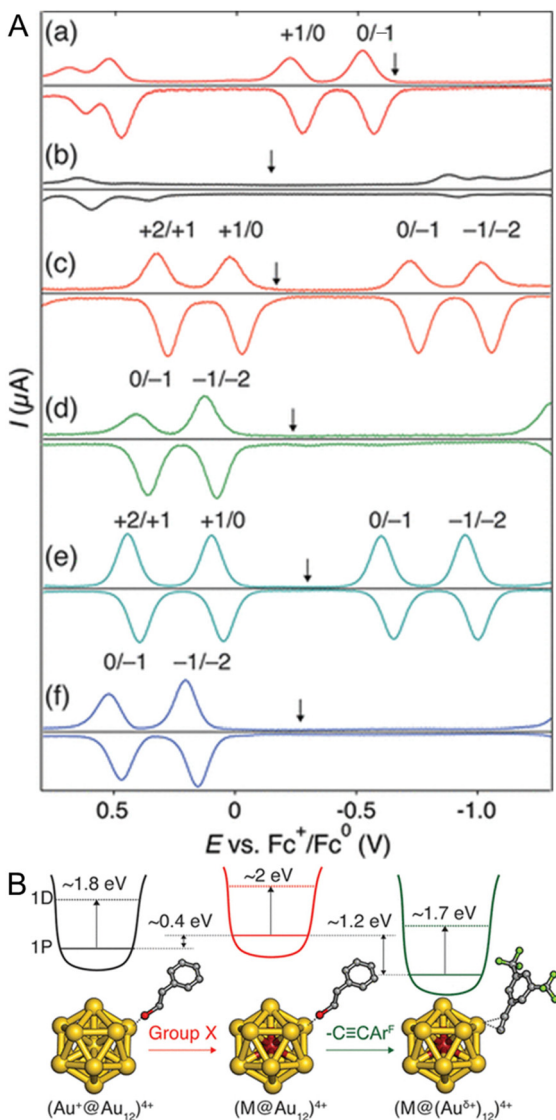


Fig. 8 (A) Differential pulse voltammograms of (a)  $[\text{Au}_{25}(\text{PET})_{18}]^-$ , (b)  $[\text{Au}_{25}(\text{C}\equiv\text{CAr}^{\text{F}})_{18}]^-$ , (c)  $[\text{PdAu}_{24}(\text{PET})_{18}]^0$ , (d)  $[\text{PdAu}_{24}(\text{C}\equiv\text{CAr}^{\text{F}})_{18}]^{2-}$ , (e)  $[\text{PtAu}_{24}(\text{PET})_{18}]^0$ , and (f)  $[\text{PtAu}_{24}(\text{C}\equiv\text{CAr}^{\text{F}})_{18}]^{2-}$  in a  $\text{CH}_2\text{Cl}_2$  solution of 0.1 M  $\text{TBAPF}_6$  at room temperature. The down arrows indicate the corresponding open-circuit potentials. (B) Schematic energy diagram of  $\text{M}@\text{Au}_{12}$  superatoms protected by thiolate or alkynyl groups. Reproduced with permission from ref. 104. Copyright 2019, American Chemical Society.

Solvent–ligand interactions also have an important effect on the electrochemically obtained H–L gap. Kwak and Lee<sup>108</sup> investigated the H–L gaps of water-soluble  $\text{Au}_{25}(\text{MPS})_{18}$  ((3-mercaptopropyl)sulfonate) and  $[\text{Au}_{25}(\text{SC}_6\text{H}_{13})_{18}]^-$  by optical and electrochemical methods (Fig. 9A and B). Electrochemically, SWV measurements in  $\text{CH}_2\text{Cl}_2$  containing 0.1 M  $\text{TBAPF}_6$  were performed. For  $[\text{Au}_{25}(\text{SC}_6\text{H}_{13})_{18}]^-$ , a H–L gap of 1.65 V was obtained, whereas the H–L gap for  $\text{Au}_{25}(\text{MPS})_{18}$  was 1.39 V. The O1–O2 gap difference was not very large, suggesting that the dielectric environments were not significantly different in the NCs. Furthermore, the ratio of the  $\text{CH}_2\text{Cl}_2$ /toluene solvent mixture was varied, and SWV measurements were performed in these solvents (Fig. 9A and B). In  $[\text{Au}_{25}(\text{SC}_6\text{H}_{13})_{18}]^-$ , the H–L gap did not change when the ratio of the mixed solvent was changed (Fig. 9B). However, for  $\text{Au}_{25}(\text{MPS})_{18}$ , the first reduction potential ( $R1$ ) shifted in the negative potential direction as the proportion of toluene increased. As a result, the H–L gap shifted from 1.39 to 1.66 V, which was found to be in close agreement with  $[\text{Au}_{25}(\text{SC}_6\text{H}_{13})_{18}]^-$  (Fig. 9A). This solvent dependence can be explained by the electrostatic effects of the MPS ligand and  $\text{TOA}^+$  ( $\text{TOA} = \text{tetraoctylammonium}$ ): the  $\text{SO}_3^-$  group of the MPS ligand produces an ion-pair interaction with  $\text{TOA}^+$ , resulting in depolarisation. Furthermore, depolarisation is expected to be influenced by the solvent polarity, which affects the strength of the ion-pair interaction between the  $\text{SO}_3^-$  group and  $\text{TOA}^+$ . As a result, more positive charge is induced in the Au core by the polarised  $\text{SO}_3^-$  group, which may result in a positive redox potential shift in  $\text{Au}_{25}(\text{MPS})_{18}$ . Similarly, the charging energy is known to vary with the solvent, even when only hydrophobic ligands are used. These effects of the ligand and solvent interactions on the H–L gap and charging energies might be better understood when the details of how solvation occurs between the SR ligands and solvents surrounding  $\text{Au}_n(\text{SR})_m$  NCs are further clarified.

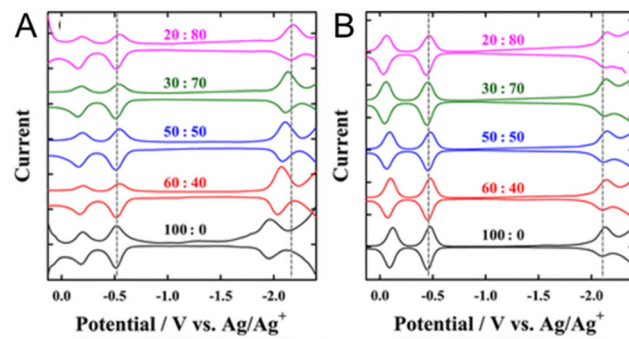


Fig. 9 Square-wave voltammograms of (A)  $\text{Au}_{25}(\text{MPS})_{18}$  and (B)  $[\text{Au}_{25}(\text{SC}_6\text{H}_{13})_{18}]^-$  in  $\text{CH}_2\text{Cl}_2$ /toluene mixtures containing 0.1 M  $\text{TBAPF}_6$ . The  $\text{CH}_2\text{Cl}_2$ /toluene compositions (v/v) are indicated on the voltammograms. The first oxidation and reduction potentials of  $\text{Au}_{25}(\text{MPS})_{18}$  in 20 : 80  $\text{CH}_2\text{Cl}_2$ /toluene are indicated by dashed lines for comparison. Reproduced with permission from ref. 108. Copyright 2012, American Chemical Society.

### 3.5 Doping effect on the electronic structure of thiolate-protected gold nanoclusters

For  $\text{Au}_{25}(\text{SR})_{18}$ , there are a number of different elements (Ag, Cd, Cu, Hg, Ir, Pd, and Pt) that can be substituted for the Au atoms, and these are the most widely studied doped  $\text{Au}_n(\text{SR})_m$  NCs. These  $\text{Au}_{25-x}\text{M}_x(\text{SR})_{18}$  alloys can be divided into three groups: (i) a group with Pt or Pd, (ii) a group with Ag or Cu, and (iii) a group with Hg or Cd as the heteroatom. For NCs in group (i), neutral  $[\text{Au}_{24}\text{M}_1(\text{SR})_{18}]^0$  ( $\text{M} = \text{Pt}$  or  $\text{Pd}$ ) with a total valence electron number of six can be stably synthesized.<sup>109,110</sup> However, the NCs in group (ii) are stably synthesised as negative  $[\text{Au}_{25-x}\text{M}_x(\text{SR})_{18}]^-$  ( $\text{M} = \text{Ag}$  or  $\text{Cu}$ ) NCs, and those in group (iii) are neutral  $[\text{Au}_{25-x}\text{M}_x(\text{SR})_{18}]^0$  ( $\text{M} = \text{Hg}$  or  $\text{Cd}$ ) NCs with a total number of eight valence electrons. The difference in the total number of valence electrons in such  $\text{Au}_{25-x}\text{M}_x(\text{SR})_{18}$  NCs induces significant changes of the energy level in their HOMOs and LUMOs. Consequently, optical absorption of  $\text{Au}_{25-x}\text{M}_x(\text{SR})_{18}$  ( $\text{M} = \text{Ag}$ ,  $\text{Cd}$ ,  $\text{Cu}$ ,  $\text{Hg}$ ,  $\text{Pd}$  or  $\text{Pt}$ ) significantly differs between the six- and eight-electron systems. The six-electron system shows a smaller H-L gap than the eight-electron system.

In 2012, Negishi and co-workers.<sup>111</sup> optically and electrochemically determined the electronic structures of  $[\text{Au}_{25-x}\text{Cu}_x(\text{PET})_{18}]^-$  ( $x = 1-5$ ) (Fig. 10). By DPV measurements, for  $[\text{Au}_{25}(\text{PET})_{18}]^-$ , the redox peaks corresponding to  $[\text{Au}_{25}(\text{PET})_{18}]^{-1/0}$  and  $[\text{Au}_{25}(\text{PET})_{18}]^{-2/-1}$  were observed at  $-282$  (O1) and  $-1942$  mV (R1) *vs.* ferrocene (Fc)<sup>+1/0</sup>, respectively (Fig. 10B). For  $[\text{Au}_{25-x}\text{Cu}_x(\text{PET})_{18}]^-$  ( $x = 1-5$ ), the peaks were observed at more positive energies ( $-276$  (O1) and  $-1896$  (R1) mV *vs.* Fc<sup>+1/0</sup>). This indicates that Cu doping decreases the HOMO and LUMO energies of  $[\text{Au}_{25}(\text{PET})_{18}]^-$ . The LUMO shift (46 mV) was larger than the HOMO shift (6 mV), indicating that Cu doping decreases the H-L gap. DFT calculations showed that Cu doped at the stable site does not significantly change the H-L gap, whereas Cu doped at the core surface site decreases the H-L gap.

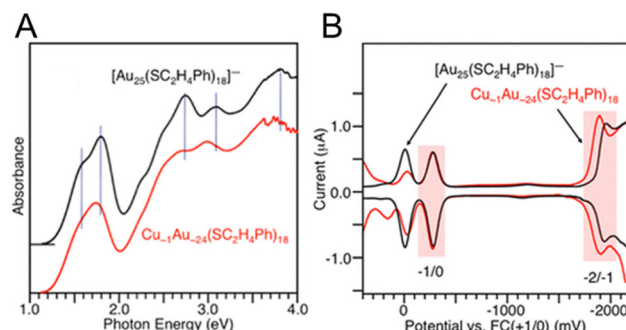


Fig. 10 (A) Optical absorption spectra of  $\text{Cu}_{-1}\text{Au}_{-24}(\text{PET})_{18}$  and  $[\text{Au}_{25}(\text{PET})_{18}]^-$ . The dotted lines indicate the main peak positions in the absorption spectrum of  $[\text{Au}_{25}(\text{PET})_{18}]^-$ . (B) DPV curves of  $\text{Cu}_{-1}\text{Au}_{-24}(\text{PET})_{18}$  and  $[\text{Au}_{25}(\text{PET})_{18}]^-$ . The red shaded regions indicate the peaks derived from the redox potentials of  $-2/-1$  and  $-1/0$ . Reproduced with permission from ref. 111. Copyright 2012, American Chemical Society.

In 2019, Maran and co-workers<sup>112</sup> revealed the electronic structures of  $\text{Au}_{24}\text{M}(\text{SR})_{18}$  ( $\text{M} = \text{Au}$ ,  $\text{Cd}$ ,  $\text{Hg}$  and  $\text{Pt}$ ) by DPV measurements (Fig. 11A). Electrochemical measurements were performed using a glassy carbon microdisc electrode in  $\text{CH}_2\text{Cl}_2$  containing 0.1 M TBAPF<sub>6</sub>. The DPV curves of  $[\text{Au}_{24}\text{Hg}(\text{SC}_4\text{H}_9)_{18}]^0$  and  $[\text{Au}_{24}\text{Cd}(\text{SC}_4\text{H}_9)_{18}]^0$  were qualitatively similar: two successive one-electron oxidations ( $E_1^\circ$  for O1 and  $E_2^\circ$  for O2) were observed at 0.364 and 0.684 V *vs.* SCE for  $[\text{Au}_{24}\text{Hg}(\text{SC}_4\text{H}_9)_{18}]^0$  and at 0.332 and 0.636 V *vs.* SCE for  $[\text{Au}_{24}\text{Cd}(\text{SC}_4\text{H}_9)_{18}]^0$ . On the timescale of the voltammetry experiments, both reactions were reversible processes. The first peaks were observed on the more positive side for  $[\text{Au}_{24}\text{Hg}(\text{SC}_4\text{H}_9)_{18}]^0$  and  $[\text{Au}_{24}\text{Cd}(\text{SC}_4\text{H}_9)_{18}]^0$  compared with those for  $[\text{Au}_{25}(\text{SC}_4\text{H}_9)_{18}]^-$  ( $E_1^\circ = -0.188$  and  $E_2^\circ = 0.139$  V *vs.* SCE). A similar trend was observed using the PET ligand instead of the  $\text{SC}_4\text{H}_9$  ligand. The first reduction peaks (R1) were observed at  $-1.23$  and  $-1.39$  V *vs.* SCE for  $[\text{Au}_{24}\text{Hg}(\text{SC}_4\text{H}_9)_{18}]^0$  and  $[\text{Au}_{24}\text{Cd}(\text{SC}_4\text{H}_9)_{18}]^0$ , respectively. These anion formation processes were chemically irreversible, in which case the potential can be detected reversibly by increasing the potential scanning rate. The H-L gap of  $[\text{Au}_{24}\text{Cd}(\text{SC}_4\text{H}_9)_{18}]^0$  was determined to be 1.41 eV, which was in good agreement with the H-L gap of 1.37 eV determined by optical absorption (Fig. 11B). Similarly, the H-L gap of  $[\text{Au}_{24}\text{Cd}(\text{PET})_{18}]^0$  was determined to be 1.46 eV, which was in good agreement with the H-L gap of 1.41 eV determined by optical absorption (Fig. 11B). Furthermore, a

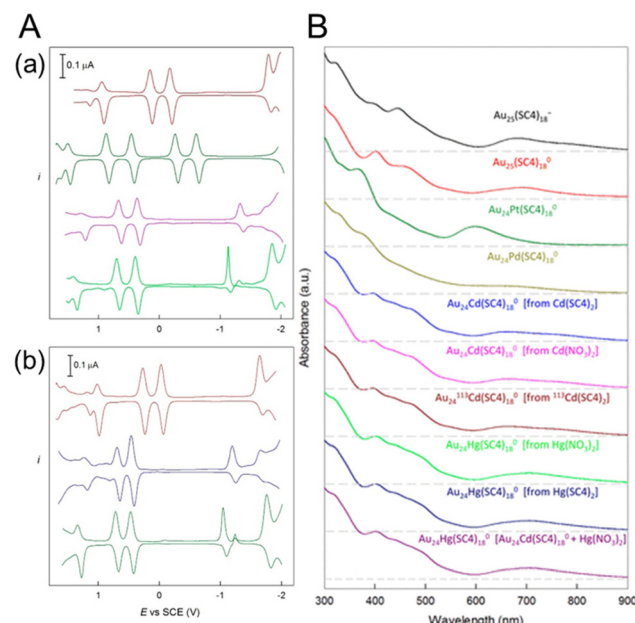
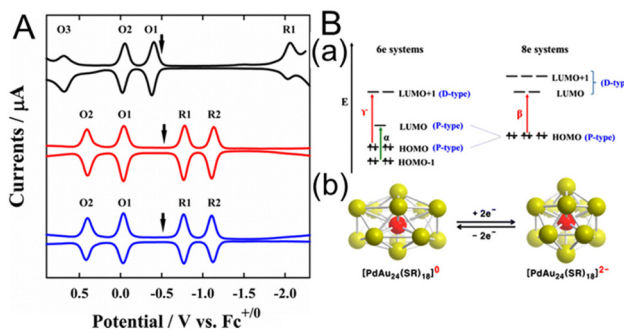


Fig. 11 (A) Comparison of the DPV curves of (from top to bottom) (a)  $[\text{Au}_{25}(\text{SC}_4\text{H}_9)_{18}]^-$ ,  $[\text{Au}_{24}\text{Pt}(\text{SC}_4\text{H}_9)_{18}]^0$ ,  $[\text{Au}_{24}\text{Cd}(\text{SC}_4\text{H}_9)_{18}]^0$ , and  $[\text{Au}_{24}\text{Hg}(\text{SC}_4\text{H}_9)_{18}]^0$  and (b)  $[\text{Au}_{25}(\text{PET})_{18}]^-$ ,  $[\text{Au}_{24}\text{Cd}(\text{PET})_{18}]^0$ , and  $[\text{Au}_{24}\text{Hg}(\text{PET})_{18}]^0$  (glassy-carbon electrode,  $\text{CH}_2\text{Cl}_2/0.1$  M TBAH,  $25$  °C). (B) Ultraviolet-visible absorption spectra of all of the  $\text{SC}_4\text{H}_9$ -protected samples ( $0.2$  mM,  $1$  mm cuvette) in  $\text{CH}_2\text{Cl}_2$ . For better comparison, the curves have been shifted vertically. The dashed lines indicate the corresponding zero absorbance. Reproduced with permission from ref. 112. Copyright 2019, American Chemical Society.



decrease in the H-L gap was observed for Hg doping. The change of the H-L gap with Hg doping has also been reported by Yang, Wu and co-workers,<sup>113</sup> but the H-L gap difference was not as large as the differences in the Pt- and Pd-doped six-electron systems.

In 2015, Lee and co-workers<sup>110</sup> investigated the electronic structures of  $[\text{Au}_{24}\text{Pt}(\text{PET})_{18}]^0$  and  $[\text{Au}_{24}\text{Pd}(\text{PET})_{18}]^0$  (Fig. 12A). For  $[\text{Au}_{24}\text{Pd}(\text{PET})_{18}]^0$ , the open-circuit potential was in the middle of the two redox peaks (O1 and R1) at  $-0.48$  V vs.  $\text{Fc}^{+/0}$ , indicating that it was neutral. Furthermore, the electrochemical gap between O1 and R1 was  $0.75$  V, giving a H-L gap of  $0.32$  V when the charge energy (O1–O2,  $0.43$  V) was considered. This was a dramatic decrease from the H-L gap of  $1.32$  eV for  $[\text{Au}_{25}(\text{PET})_{18}]^-$ .  $[\text{Au}_{24}\text{Pt}(\text{PET})_{18}]^0$  showed a similar trend, with a H-L gap of  $0.32$  eV, indicating that  $[\text{Au}_{24}\text{Pt}(\text{PET})_{18}]^0$  and  $[\text{Au}_{24}\text{Pd}(\text{PET})_{18}]^0$  have very similar electronic states (Fig. 12A). To investigate the origin of the small H-L gap, DFT calculations were performed to simulate the energy levels of the six- and eight-electron systems (Fig. 12B).  $[\text{Au}_{25}(\text{SCH}_3)_{18}]^-$ ,  $[\text{Au}_{24}\text{Pd}(\text{SCH}_3)_{18}]^{2-}$ , and  $[\text{Au}_{24}\text{Pt}(\text{SCH}_3)_{18}]^{2-}$  exhibit stable superatomic eight-electron systems ( $1\text{S}^21\text{P}^6$ ), whereas the six-electron systems, including  $[\text{Au}_{24}\text{Pd}(\text{SCH}_3)_{18}]^0$  and  $[\text{Au}_{24}\text{Pt}(\text{SCH}_3)_{18}]^0$ , have two electrons less than eight-electron systems. Therefore, they split from a triple degenerate HOMO into a doubly degenerate HOMO and LUMO, functioning as a superatomic  $1\text{P}$  orbital (Fig. 12B). The H-L gap cannot be determined from the optical absorption spectrum because the dipole selection rule forbids optical HOMO–LUMO transitions. However, the H-L gaps of  $[\text{Au}_{24}\text{Pt}(\text{PET})_{18}]^0$  and  $[\text{Au}_{24}\text{Pd}(\text{PET})_{18}]^0$  can be revealed by SWV, because they are not forbidden electrochemically. Therefore, this electrochemical method is particularly useful for  $\text{Au}_n(\text{SR})_m$ , where the HOMO–LUMO



**Fig. 12** (A) Square-wave voltammograms of  $[\text{Au}_{25}(\text{SC}_6\text{H}_{13})_{18}]^-$  (black),  $[\text{PdAu}_{24}(\text{SC}_6\text{H}_{13})_{18}]^0$  (red), and  $[\text{PtAu}_{24}(\text{SC}_6\text{H}_{13})_{18}]^0$  (blue). The electrochemical measurements were performed in  $\text{CH}_2\text{Cl}_2$  containing  $0.1$  M TBAPF<sub>6</sub>. The arrows indicate the solution open-circuit potentials. (B) (a) Electronic energy levels of the six-electron and eight-electron systems.  $\alpha$ ,  $\beta$ , and  $\gamma$  denote the optical transitions occurring in the six- and eight-electron systems. (b) Schematic showing Jahn–Teller-like distortion in the core (e.g.,  $\text{PdAu}_{12}$ ) predicted for six-electron  $[\text{PdAu}_{24}(\text{SR})_{18}]^0$  (left), which undergoes a structural change to nearly spherical eight-electron  $[\text{PdAu}_{24}(\text{SR})_{18}]^{2-}$  upon reduction (right). The vertical compression of  $[\text{PdAu}_{24}(\text{SR})_{18}]^0$  (left) is exaggerated. Reproduced with permission from ref. 110. Copyright 2015, American Chemical Society.

transition is optically forbidden. In addition, they reported the doping effects of Pt and Pd atoms for  $\text{Au}_{38}(\text{SR})_{24}$ .<sup>114</sup> The H-L gap of  $[\text{Au}_{36}\text{Pt}_2(\text{SC}_6\text{H}_{13})_{24}]^{2-}$  measured by voltammetry was slightly larger than that of undoped  $[\text{Au}_{38}(\text{SC}_6\text{H}_{13})_{24}]^0$ , whereas the H-L gap of  $[\text{Au}_{36}\text{Pd}_2(\text{SC}_6\text{H}_{13})_{24}]^0$  was significantly smaller ( $0.26$  V), resulting in the appearance of a near-infrared band at  $\sim 0.8$  eV.

The change in the H-L gap has also been determined by electrochemical methods for doping with multiple different atoms. In 2020, Negishi and co-workers<sup>115</sup> determined the H-L gaps of  $[\text{Au}_{24}\text{Pt}(\text{SR})_{18}]^0$  and  $[\text{Au}_{24-x}\text{PtCu}_x(\text{PET})_{18}]^0$  by DPV measurements (Fig. 13A). The H-L gap of the NC hardly changed by Cu substitution (Fig. 13A–C). The states of the HOMO and LUMO in  $[\text{Au}_{24}\text{Pt}(\text{SR})_{18}]^0$  are caused by the dissolution of the degenerate electronic states owing to the symmetry lowering of the metal core (Fig. 13C, Jahn–Teller effect).<sup>39</sup> It was presumed that substitution of Cu at the core surface Au did not significantly change the magnitude of the strain in the metal core, resulting in the H-L gap hardly changing. In 2020, Tsukuda and co-workers<sup>116</sup> revealed the electronic structure of  $[\text{Au}_{23}\text{PtCd}(\text{PET})_{18}]^-$  by optical spectroscopy and electrochemical measurements (Fig. 14A and B). The first and second oxidation potentials (O1 and O2) of  $[\text{Au}_{23}\text{PtCd}(\text{PET})_{18}]^-$  were  $0.110$  and  $0.175$  V higher than those of  $[\text{Au}_{25}(\text{PET})_{18}]^-$ , respectively (Fig. 14B). This indicates that the  $1\text{P}$  superatomic orbitals of Pt@CdAu<sub>11</sub> in  $[\text{Au}_{23}\text{PtCd}(\text{PET})_{18}]^-$  are slightly more stable than those of Au@Au<sub>12</sub> in  $[\text{Au}_{25}(\text{PET})_{18}]^-$ . The electrochemically determined H-L gap of  $[\text{Au}_{23}\text{PtCd}(\text{PET})_{18}]^-$  was  $1.45$  eV, which was in good agreement with the optically determined H-L gap ( $1.41$  eV). This is sig-

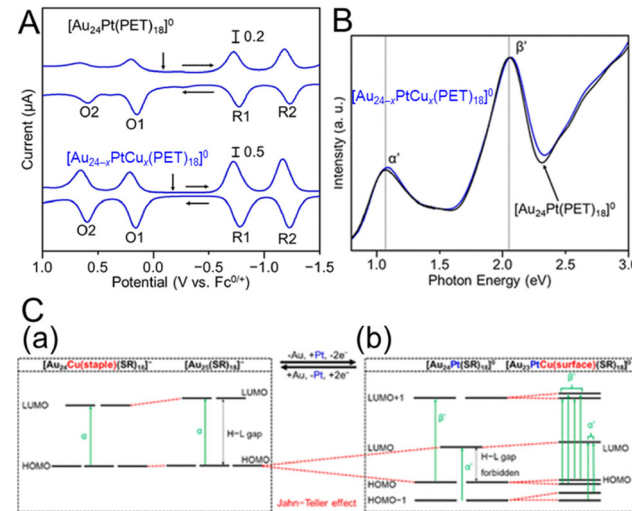


**Fig. 13** (A) DPV curves of  $[\text{Au}_{24}\text{Pt}(\text{PET})_{18}]^0$  and  $[\text{Au}_{24-x}\text{PtCu}_x(\text{PET})_{18}]^0$  ( $x = 0.9$ ). The vertical arrows indicate the solution open-circuit potentials, and the horizontal arrows indicate the scan direction. (B) Optical absorption spectra of  $[\text{Au}_{24-x}\text{PtCu}_x(\text{PET})_{18}]^0$  ( $x = 0.9$ ) (blue) and  $[\text{Au}_{24}\text{Pt}(\text{PET})_{18}]^0$  (black). (C) Schematic of the effect of Cu substitution on the electronic structure of (a)  $[\text{Au}_{25-x}\text{Cu}_x(\text{SR})_{18}]^-$  and (b)  $[\text{Au}_{24-x}\text{PtCu}_x(\text{SR})_{18}]^0$ . Reproduced with permission from ref. 115. Copyright 2020, American Chemical Society.

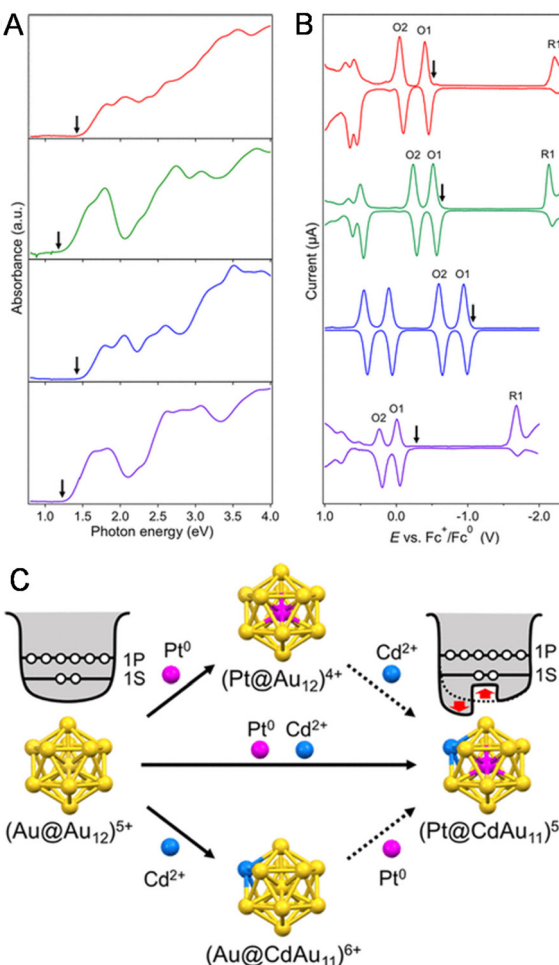


**Fig. 14** (A) Ultraviolet–visible–near-infrared spectra and (B) DPV curves of  $[Au_{23}PtCd(PET)_{18}]^-$  (red),  $[Au_{25}(PET)_{18}]^-$  (green),  $[Au_{24}Pt(PET)_{18}]^0$  (blue), and  $[Au_{24}Cd(PET)_{18}]^0$  (purple) in benzene and  $CH_2Cl_2$ , respectively. The downward arrows in panels (A) and (B) represent the corresponding optical H–L gaps and open-circuit potentials, respectively. (C) Schematic illustration of the jellium potentials of the  $(Au@Au_{12})^{5+}$  and  $(Pt@CdAu_{11})^{5+}$  superatoms. Reproduced with permission from ref. 116. Copyright 2020, American Chemical Society.

nificantly larger than the H–L gap (1.30 eV) of  $[Au_{25}(PET)_{18}]^-$ . However, the H–L gap of  $[Au_{24}Cd(PET)_{18}]^0$  (1.29 eV) was almost the same as that of  $[Au_{25}(PET)_{18}]^-$ . The H–L gap of the  $Pt@CdAu_{11}$  superatomic core is larger than that of  $Au@Au_{12}$ , mainly because of Pt doping at the centre (Fig. 14C), which is in good agreement with the electronic structure changes observed by optical absorption spectroscopy and electrochemical measurements.

The Ag replacing effect on the electronic structure of  $Au_n(SR)_m$  was also investigated by Dass and co-workers.<sup>90</sup> using  $Au_{144-x}Ag_x(PET)_{60}$  ( $x = 46$ ). The electrochemical gap of  $Au_{144}(PET)_{60}$  was approximately 0.37 V, while that of  $Au_{144-x}Ag_x(PET)_{60}$  was approximately 0.38 V. A previous study of the band gap of  $Au_{144-x}Ag_x(PET)_{60}$  using a combination of optical absorption spectroscopy and DFT calculations showed that the optical band gap is only moderately affected by Ag

doping in this size range,<sup>117</sup> which was consistent with previous reports.

In summary, previous studies indicate that doping the centre of  $Au_{25}(SR)_{18}$  with Pt or Pd as a heteroatom has a significant effect on the electronic structure. It is expected that doping multiple elements can create an even greater variety of electronic states if the doping positions of the different elements can be controlled. The effects of doping with different elements have been found to be more pronounced for  $Au_n(SR)_m$  with smaller size.

### 3.6 Geometric structure effect on the electronic structure of thiolate-protected gold nanoclusters

Park and Lee<sup>101</sup> compared the electronic states of  $Au_{25}$  NCs with two  $Au_{13}$  icosahedra connected *via* vertex sharing ( $[Au_{25}(PPh_3)_{10}(SC_6H_{13})_5Cl_2]^{2+}$ ) and one  $Au_{13}$  icosahedral core ( $[Au_{25}(SC_6H_{13})_{18}]^-$ ) (Fig. 15). In this case, a series of  $[Au_{25}(PPh_3)_{10}(SR)_5Cl_2]^{2+}$  NCs protected with SR (SR =  $SC_6H_{13}$ , PET, 11-hydroxy-1-undecanethiolate (MU), and 10-carboxy-1-decanethiolate (MUA)) was prepared. SWV measurements were performed with  $[Au_{25}(SC_6H_{13})_{18}]^-$  and  $[Au_{25}(PPh_3)_{10}(SC_6H_{13})_5Cl_2]^{2+}$  in 0.1 M TBAPF<sub>6</sub>/CH<sub>2</sub>Cl<sub>2</sub> at –78 °C. The results showed that the open-circuit potential of the solution of  $[Au_{25}(PPh_3)_{10}(SC_6H_{13})_5Cl_2]^{2+}$  was approximately 0.37 V vs. 1,4-benzoquinone (BQ)<sup>–/0</sup>, and a series of oxidation peaks at 0.91 V (O1), 1.13 V (O2), 1.45 V (O3), and 1.62 V (O4) vs. BQ<sup>–/0</sup> was observed, corresponding to oxidation of +3, +4, +5, and +6 for  $[Au_{25}(PPh_3)_{10}(SC_6H_{13})_5Cl_2]^{2+}$ , respectively (Fig. 15B). From this voltammogram, the electrochemical energy gap was determined to be 1.54 V from the difference between the initial oxidation (O1) and reduction (R1) potentials (Fig. 15B). Compared with  $[Au_{25}(SC_6H_{13})_{18}]^-$ , the oxidation and reduction peaks (O1 and R1) of  $[Au_{25}(PPh_3)_{10}(SC_6H_{13})_5Cl_2]^{2+}$  were observed at significantly

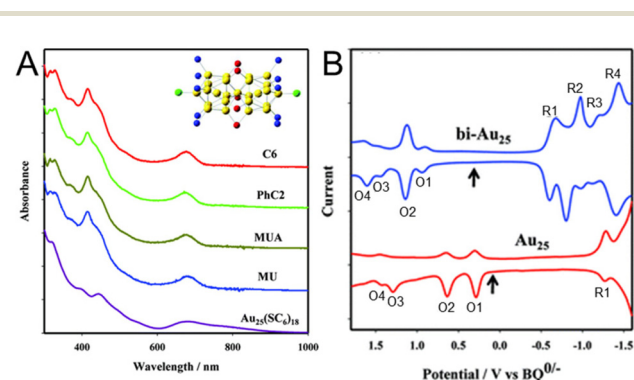


**Fig. 15** (A) Absorption spectra of  $[Au_{25}(PPh_3)_{10}(SR)_5Cl_2]^{2+}$  (SR =  $SC_6H_{13}$ , PET, MUA, and MU) and  $Au_{25}(SC_6H_{13})_{18}$  in  $CH_2Cl_2$ . All of the spectra have been normalized to unity at 300 nm and offset for clarity. The insert shows the core structure of  $Au_{25}(PPh_3)_{10}(SR)_5Cl_2$ . (B) Square-wave voltammograms of  $[Au_{25}(PPh_3)_{10}(SC_6H_{13})_5Cl_2]^{2+}$  (top) and  $[Au_{25}(SC_6H_{13})_{18}]^-$  (bottom) in 0.1 M TBAPF<sub>6</sub> in degassed  $CH_2Cl_2$  at –78 °C. The arrows indicate the solution open-circuit potentials. The open-circuit potential of  $Au_{25}$  indicates that the  $Au_{25}$  NC is an anionic form,  $[Au_{25}(SC_6H_{13})_{18}]^-$ . The concentration of  $[Au_{25}(PPh_3)_{10}(SC_6H_{13})_5Cl_2]^{2+}$  was 4 mg mL<sup>–1</sup>, and the tick interval on the current axis is 0.2  $\mu$ A. Reproduced with permission from ref. 101. Copyright 2012, American Chemical Society.



more positive potentials. The electrochemical energy gap of  $[\text{Au}_{25}(\text{PPh}_3)_{10}(\text{SC}_6\text{H}_{13})_5\text{Cl}_2]^{2+}$  (1.54 V) was smaller than that of  $[\text{Au}_{25}(\text{SC}_6\text{H}_{13})_{18}]^-$  (1.65 V), indicating that these NCs had clearly different electronic energy structures. The electrochemical energy gap of  $[\text{Au}_{25}(\text{PPh}_3)_{10}(\text{SC}_6\text{H}_{13})_5\text{Cl}_2]^{2+}$  was also smaller than that of the icosahedral  $\text{Au}_{13}$  NC assigned to  $\text{Au}_{13}(\text{PPh}_3)_4(\text{SC}_{12}\text{H}_{25})_2\text{Cl}_2$  (1.76 V).<sup>69</sup> Furthermore, the potential gap between O2 and O3 (0.32 V) was significantly smaller than the potential gap of  $[\text{Au}_{25}(\text{SC}_6\text{H}_{13})_{18}]^-$  (0.65 V). From the difference between the O2–O3 gap and O1–O2 gap, the charging energy of 0.10 eV was obtained. The electronic energy levels adjacent to the HOMO of  $[\text{Au}_{25}(\text{PPh}_3)_{10}(\text{SC}_6\text{H}_{13})_5\text{Cl}_2]^{2+}$  were revealed to be degenerate or close to each other owing to their high symmetry.<sup>118</sup> Although there were differences in their charge states and some ligands, such as SRs, phosphines, and halogens, in the  $\text{Au}_{25}$  NCs with different geometries, the difference in their electronic structures was revealed. Furthermore, for such  $[\text{Au}_{25}(\text{PPh}_3)_{10}(\text{SR})_5\text{Cl}_2]^{2+}$  NCs, it has been reported that Pd doping decreases the H–L gap owing to splitting of the degenerate HOMO.<sup>119</sup>

The effect of the  $\text{Au}_n(\text{SR})_m$  core structure on the electrochemical gap was investigated by Wu and co-workers.<sup>120</sup> The electronic structures of  $\text{Au}_{28}(\text{S-c-C}_6\text{H}_{11})_{20}$  (S-c-C<sub>6</sub>H<sub>11</sub> = cyclohexanethiolate),  $\text{Au}_{28}(\text{TBBT})_{20}$ ,  $\text{Au}_{25}(\text{PET})_{18}$ ,  $\text{Au}_{44}(\text{DMBT})_{26}$  (DMBT = 2,4-dimethylbenzenethiolate),  $\text{Au}_{44}(\text{TBBT})_{28}$ ,  $\text{Au}_{49}(\text{DMBT})_{27}$ ,  $\text{Au}_{38}(\text{PET})_{24}$ , and  $\text{Au}_{36}(\text{TBBT})_{24}$  were investigated. The results showed that the  $\text{Au}_n(\text{SR})_m$  NC with a kernel of the fcc structure has a larger electrochemical gap than the  $\text{Au}_n(\text{SR})_m$  NC with a kernel of the non-fcc structure.

## 4 Conclusions and outlook

Electrochemical techniques can be used to determine the H–L gaps of metal NCs, and the electronic structures of various  $\text{Au}_n(\text{SR})_m$  have been elucidated by electrochemical measurements, as well as by optical absorption spectroscopy and DFT calculations. Bulk Au does not have a band gap, but a molecule-like H–L gap forms in small  $\text{Au}_n(\text{SR})_m$  NCs, and the H–L gap tends to increase with decreasing size.  $\text{Au}_{25}(\text{SR})_{18}$  is currently the most studied  $\text{Au}_n(\text{SR})_m$  NC. In  $\text{Au}_{25}(\text{SR})_{18}$ , molecular changes of R in the SR ligand do not significantly change the H–L gap, but the electronic state greatly changes when S is a different atom or group (e.g., Se, Te, and C≡CR). Substitution of different elements for Au (i.e., alloying) also changes the H–L gap. In particular, substitution of Pt or Pd for Au in  $\text{Au}_{25}(\text{SR})_{18}$  significantly reduces the H–L gap owing to dissolution of the degeneracy of the electronic states. Furthermore, in  $\text{Au}_n(\text{SR})_m$ , where the HOMO–LUMO transition is optically forbidden, the H–L gaps, which cannot be calculated from the optical spectra, can be determined by electrochemical methods.

These electrochemical methods have also been applied to Au NCs protected by phosphine<sup>121–128</sup> and stibine,<sup>129</sup> and to NCs based on Ag,<sup>130–133</sup> Cu,<sup>134</sup> and group 10 elements.<sup>135–139</sup> In the future, these electrochemical techniques are expected to

reveal the electronic states of metal NCs protected by other ligands and composed of other metals.<sup>140–144</sup>

The electrochemical gap also varies depending on the ligand, solvent, electrolyte, measurement mode, temperature, and other factors. This is also the same when determining the H–L gaps from optical absorption spectra, and care should be taken when comparing the H–L gap values obtained in different studies. More accurate H–L gap calculations are required through the development of models that more accurately take the charging energy into account and a unified measurement method.<sup>61,145,146</sup>

The electronic structures of  $\text{Au}_n(\text{SR})_m$  NCs in solution have already been extensively studied. However, it is desirable to clarify the electronic states of  $\text{Au}_n(\text{SR})_m$  NCs on catalyst supports when considering their use in catalytic reactions in the gas or solid phase.<sup>135,147–151</sup> In this case, it is expected that the electronic/geometric state of  $\text{Au}_n(\text{SR})_m$  NCs will also significantly change during catalytic reaction. For instance, ligands have also been reported to desorb from  $\text{Au}_n(\text{SR})_m$  NCs upon applying potential<sup>152</sup> and the catalytic properties to be depends on the electronic state of  $\text{Au}_n(\text{SR})_m$  NCs.<sup>153</sup> It is expected that techniques such as pulse voltammetry can be used to elucidate the mechanism of such electrochemical catalytic reactions. If the electronic states of  $\text{Au}_n(\text{SR})_m$  NCs during catalytic reaction could be investigated, it would be possible to clarify the details of the catalytic reaction mechanisms predicted by theoretical calculations.<sup>154</sup> It is expected that the electronic states of various  $\text{Au}_n(\text{SR})_m$  NCs will be clarified by electrochemical methods and these measurement techniques will be further developed in the future.

## Conflicts of interest

There are no conflicts to declare.

## Acknowledgements

This work was supported by the Japan Society for the Promotion of Science (JSPS) KAKENHI (grant numbers 20H02698 and 20H02552), Scientific Research on Innovative Areas “Innovations for Light-Energy Conversion” (grant numbers 18H05178 and 20H05115), Scientific Research on Innovative Areas “Hydrogenomics” (grant number 21H00027), and the Joint Usage/Research Center for Catalysis (proposal numbers 22AY0056 and 23AY0189). Funding from the Takahashi Industrial and Economic Research Foundation, the Yazaki Memorial Foundation for Science and Technology, the Ogasawara Foundation for the Promotion of Science and Engineering, the Kao Foundation for Arts and Sciences, a Sasakawa Scientific research grant from the Japan Science Society, a TEPCO Memorial Foundation research grant (Basic Research), Advanced Technology Institute research grants 2022, and the Kumagai Foundation for Science and Technology are gratefully acknowledged.



## References

- 1 R. Jin, C. Zeng, M. Zhou and Y. Chen, *Chem. Rev.*, 2016, **116**, 10346.
- 2 I. Chakraborty and T. Pradeep, *Chem. Rev.*, 2017, **117**, 8208.
- 3 R. R. Nasaruddin, T. Chen, N. Yan and J. Xie, *Coord. Chem. Rev.*, 2018, **368**, 60.
- 4 Y. Du, H. Sheng, D. Astruc and M. Zhu, *Chem. Rev.*, 2020, **120**, 526.
- 5 K. Yamamoto, T. Imaoka, M. Tanabe and T. Kambe, *Chem. Rev.*, 2020, **120**, 1397.
- 6 S. Hossain, D. Hirayama, A. Ikeda, M. Ishimi, S. Funaki, A. Samanta, T. Kawawaki and Y. Negishi, *Aggregate*, 2023, **4**, e255.
- 7 B. Yin and Z. Luo, *Coord. Chem. Rev.*, 2021, **429**, 213643.
- 8 T. Kawawaki, Y. Imai, D. Suzuki, S. Kato, I. Kobayashi, T. Suzuki, R. Kaneko, S. Hossain and Y. Negishi, *Chem. – Eur. J.*, 2020, **26**, 16150.
- 9 X. Kang, Y. Li, M. Zhu and R. Jin, *Chem. Soc. Rev.*, 2020, **49**, 6443.
- 10 R. Jin, G. Li, S. Sharma, Y. Li and X. Du, *Chem. Rev.*, 2021, **121**, 567.
- 11 C. Dong, Y. Li, D. Cheng, M. Zhang, J. Liu, Y.-G. Wang, D. Xiao and D. Ma, *ACS Catal.*, 2020, **10**, 11011.
- 12 T. Kawawaki, A. Ebina, Y. Hosokawa, S. Ozaki, D. Suzuki, S. Hossain and Y. Negishi, *Small*, 2021, **17**, 2005328.
- 13 S. Maity, D. Bain and A. Patra, *Nanoscale*, 2019, **11**, 22685.
- 14 Z. Liu, Z. Wu, Q. Yao, Y. Cao, O. J. H. Chai and J. Xie, *Nano Today*, 2021, **36**, 101053.
- 15 H. Cui, Z.-S. Shao, Z. Song, Y.-B. Wang and H.-S. Wang, *J. Mater. Chem. C*, 2020, **8**, 14312.
- 16 X. Dou, X. Chen, H. Zhu, Y. Liu, D. Chen, X. Yuan, Q. Yao and J. Xie, *Dalton Trans.*, 2019, **48**, 10385.
- 17 A. S. K. Kumar and W.-L. Tseng, *Anal. Methods*, 2020, **12**, 1809.
- 18 S. Antonello and F. Maran, *Curr. Opin. Electrochem.*, 2017, **2**, 18.
- 19 R. W. Murray, *Chem. Rev.*, 2008, **108**, 2688.
- 20 K. Kwak and D. Lee, *Acc. Chem. Res.*, 2019, **52**, 12.
- 21 Q. Zhu, X. Huang, Y. Zeng, K. Sun, L. Zhou, Y. Liu, L. Luo, S. Tian and X. Sun, *Nanoscale Adv.*, 2021, **3**, 6330.
- 22 L. Qin, G. Ma, L. Wang and Z. Tang, *J. Energy Chem.*, 2021, **57**, 359.
- 23 Y. Sun, X. Cai, W. Hu, X. Liu and Y. Zhu, *Sci. China: Chem.*, 2021, **64**, 1065.
- 24 X. Cai, G. Li, W. Hu and Y. Zhu, *ACS Catal.*, 2022, **12**, 10638.
- 25 X. Kang and M. Zhu, *Chem. Mater.*, 2021, **33**, 39.
- 26 Y. Wang and T. Bürgi, *Nanoscale Adv.*, 2021, **3**, 2710.
- 27 W. Kurashige, Y. Niihori, S. Sharma and Y. Negishi, *Coord. Chem. Rev.*, 2016, **320–321**, 238.
- 28 C. Cesari, J.-H. Shon, S. Zucchini and L. A. Berben, *Chem. Soc. Rev.*, 2021, **50**, 9503.
- 29 V. G. Albano, P. L. Bellon, M. Manassero and M. Sansoni, *J. Chem. Soc. D*, 1970, 1210.
- 30 G. Schmid, R. Pfeil, R. Boese, F. Bandermann, S. Meyer, G. H. M. Calis and J. W. A. van der Velden, *Chem. Ber.*, 1981, **114**, 3634.
- 31 P. Chini, *J. Organomet. Chem.*, 1980, **200**, 37.
- 32 M. Paolieri, I. Ciabatti and M. Fontani, *J. Cluster Sci.*, 2019, **30**, 1623.
- 33 Y. Negishi, K. Nobusada and T. Tsukuda, *J. Am. Chem. Soc.*, 2005, **127**, 5261.
- 34 M. Brust, M. Walker, D. Bethell, D. J. Schiffrin and R. Whyman, *J. Chem. Soc., Chem. Commun.*, 1994, 801.
- 35 Y. Negishi, H. Horihata, A. Ebina, S. Miyajima, M. Nakamoto, A. Ikeda, T. Kawawaki and S. Hossain, *Chem. Sci.*, 2022, **13**, 5546.
- 36 Y. Negishi, *Phys. Chem. Chem. Phys.*, 2022, **24**, 7569.
- 37 B. Zhang, J. Chen, Y. Cao, O. J. H. Chai and J. Xie, *Small*, 2021, **17**, 2004381.
- 38 R. H. Adnan, J. M. L. Madridejos, A. S. Alotabi, G. F. Metha and G. G. Andersson, *Adv. Sci.*, 2022, **9**, 2105692.
- 39 P. D. Jazdinsky, G. Calero, C. J. Ackerson, D. A. Bushnell and R. D. Kornberg, *Science*, 2007, **318**, 430.
- 40 X. Kang and M. Zhu, *Chem. Soc. Rev.*, 2019, **48**, 2422.
- 41 H. Yu, B. Rao, W. Jiang, S. Yang and M. Zhu, *Coord. Chem. Rev.*, 2019, **378**, 595.
- 42 M.-M. Zhang, K. Li and S.-Q. Zang, *Adv. Opt. Mater.*, 2020, **8**, 1902152.
- 43 Y. Zhang, C. Zhang, C. Xu, X. Wang, C. Liu, G. I. N. Waterhouse, Y. Wang and H. Yin, *Talanta*, 2019, **200**, 432.
- 44 Y.-S. Chen, H. Choi and P. V. Kamat, *J. Am. Chem. Soc.*, 2013, **135**, 8822.
- 45 N. Sakai and T. Tatsuma, *Adv. Mater.*, 2010, **22**, 3185.
- 46 M. A. Abbas, R. Thota, K. Pyo, D. Lee and J. H. Bang, *ACS Energy Lett.*, 2020, **5**, 1404.
- 47 T. Higaki, Y. Li, S. Zhao, Q. Li, S. Li, X.-S. Du, S. Yang, J. Chai and R. Jin, *Angew. Chem., Int. Ed.*, 2019, **58**, 8291.
- 48 J. Fang, B. Zhang, Q. Yao, Y. Yang, J. Xie and N. Yan, *Coord. Chem. Rev.*, 2016, **322**, 1.
- 49 T. Kawawaki, Y. Kataoka, M. Hirata, Y. Iwamatsu, S. Hossain and Y. Negishi, *Nanoscale Horiz.*, 2021, **6**, 409.
- 50 B. Kumar, T. Kawawaki, N. Shimizu, Y. Imai, D. Suzuki, S. Hossain, L. V. Nair and Y. Negishi, *Nanoscale*, 2020, **12**, 9969.
- 51 Y. Negishi, S. Hashimoto, A. Ebina, K. Hamada, S. Hossain and T. Kawawaki, *Nanoscale*, 2020, **12**, 8017.
- 52 T. Kawawaki and Y. Negishi, *Nanomaterials*, 2020, **10**, 238.
- 53 T. Kawawaki, Y. Negishi and H. Kawasaki, *Nanoscale Adv.*, 2020, **2**, 17.
- 54 T. Kawawaki, Y. Kataoka, S. Ozaki, M. Kawachi, M. Hirata and Y. Negishi, *Chem. Commun.*, 2021, **57**, 417.
- 55 T. Kawawaki, Y. Mori, K. Wakamatsu, S. Ozaki, M. Kawachi, S. Hossain and Y. Negishi, *J. Mater. Chem. A*, 2020, **8**, 16081.
- 56 T. Ung, M. Giersig, D. Dunstan and P. Mulvaney, *Langmuir*, 1997, **13**, 1773.



57 R. S. Ingram, M. J. Hostetler, R. W. Murray, T. G. Schaaff, J. T. Khoury, R. L. Whetten, T. P. Bigioni, D. K. Guthrie and P. N. First, *J. Am. Chem. Soc.*, 1997, **119**, 9279.

58 E. Hartmann, P. Marquardt, J. Ditterich, P. Radojkovic and H. Steinberger, *Appl. Surf. Sci.*, 1996, **107**, 197.

59 S. Chen, R. S. Ingram, M. J. Hostetler, J. J. Pietron, R. W. Murray, T. G. Schaaff, J. T. Khoury, M. M. Alvarez and R. L. Whetten, *Science*, 1998, **280**, 2098.

60 J. F. Hicks, A. C. Templeton, S. Chen, K. M. Sheran, R. Jasti, R. W. Murray, J. Debord, T. G. Schaaff and R. L. Whetten, *Anal. Chem.*, 1999, **71**, 3703.

61 B. Su, M. Zhang, Y. Shao and H. H. Girault, *J. Phys. Chem. B*, 2006, **110**, 21460.

62 S. Chen and R. W. Murray, *J. Phys. Chem. B*, 1999, **103**, 9996.

63 M. J. Weaver and X. Gao, *J. Phys. Chem.*, 1993, **97**, 332.

64 S. Chen, R. W. Murray and S. W. Feldberg, *J. Phys. Chem. B*, 1998, **102**, 9898.

65 D. Lee, R. L. Donkers, J. M. DeSimone and R. W. Murray, *J. Am. Chem. Soc.*, 2003, **125**, 1182.

66 Y. Yang and S. Chen, *Nano Lett.*, 2003, **3**, 75.

67 J. F. Hicks, D. T. Miles and R. W. Murray, *J. Am. Chem. Soc.*, 2002, **124**, 13322.

68 B. M. Quinn, P. Liljeroth, V. Ruiz, T. Laaksonen and K. Kontturi, *J. Am. Chem. Soc.*, 2003, **125**, 6644.

69 L. D. Menard, S.-P. Gao, H. Xu, R. D. Tweten, A. S. Harper, Y. Song, G. Wang, A. D. Douglas, J. C. Yang, A. I. Frenkel, R. G. Nuzzo and R. W. Murray, *J. Phys. Chem. B*, 2006, **110**, 12874.

70 R. Balasubramanian, R. Guo, A. J. Mills and R. W. Murray, *J. Am. Chem. Soc.*, 2005, **127**, 8126.

71 T. Omoda, S. Takano and T. Tsukuda, *Small*, 2021, **17**, 2001439.

72 S. Jin, S. Wang and M. Zhu, *Chem. – Asian J.*, 2019, **14**, 3222.

73 R. L. Donkers, D. Lee and R. W. Murray, *Langmuir*, 2008, **24**, 5976.

74 D. Lee, R. L. Donkers, G. Wang, A. S. Harper and R. W. Murray, *J. Am. Chem. Soc.*, 2004, **126**, 6193.

75 J. Xiang, P. Li, Y. Song, X. Liu, H. Chong, S. Jin, Y. Pei, X. Yuan and M. Zhu, *Nanoscale*, 2015, **7**, 18278.

76 S. Antonello, A. H. Holm, E. Instuli and F. Maran, *J. Am. Chem. Soc.*, 2007, **129**, 9836.

77 M. Hesari, M. S. Workentin and Z. Ding, *Chem. Sci.*, 2014, **5**, 3814.

78 K. Kwak, W. Choi, Q. Tang, M. Kim, Y. Lee, D.-E. Jiang and D. Lee, *Nat. Commun.*, 2017, **8**, 14723.

79 M. Hesari, M. S. Workentin and Z. Ding, *Chem. – Eur. J.*, 2014, **20**, 15116.

80 K. N. Swanick, M. Hesari, M. S. Workentin and Z. Ding, *J. Am. Chem. Soc.*, 2012, **134**, 15205.

81 P. R. Nimmala, S. Knoppe, V. R. Jupally, J. H. Delcamp, C. M. Aikens and A. Dass, *J. Phys. Chem. B*, 2014, **118**, 14157.

82 R. Jin, C. Liu, S. Zhao, A. Das, H. Xing, C. Gayathri, Y. Xing, N. L. Rosi, R. R. Gil and R. Jin, *ACS Nano*, 2015, **9**, 8530.

83 H. Qian, Y. Zhu and R. Jin, *ACS Nano*, 2009, **3**, 3795.

84 P. R. Nimmala, B. Yoon, R. L. Whetten, U. Landman and A. Dass, *J. Phys. Chem. A*, 2013, **117**, 504.

85 V. R. Jupally, J. G. Thrasher and A. Dass, *Analyst*, 2014, **139**, 1826.

86 D. Wang, J. W. Padelford, T. Ahuja and G. Wang, *ACS Nano*, 2015, **9**, 8344.

87 P. R. Nimmala, S. Theivendran, G. Barcaro, L. Sementa, C. Kumara, V. R. Jupally, E. Apra, M. Stener, A. Fortunelli and A. Dass, *J. Phys. Chem. Lett.*, 2015, **6**, 2134.

88 K. Kwak, V. D. Thanthirige, K. Pyo, D. Lee and G. Ramakrishna, *J. Phys. Chem. Lett.*, 2017, **8**, 4898.

89 W. Choi, G. Hu, K. Kwak, M. Kim, D.-E. Jiang, J.-P. Choi and D. Lee, *ACS Appl. Mater. Interfaces*, 2018, **10**, 44645.

90 A. Dass, N. A. Sakthivel, V. R. Jupally, C. Kumara and M. Rambukwella, *ACS Energy Lett.*, 2020, **5**, 207.

91 M. Zhou, C. Zeng, Y. Song, J. W. Padelford, G. Wang, M. Y. Sfeir, T. Higaki and R. Jin, *Angew. Chem., Int. Ed.*, 2017, **56**, 16257.

92 C. Zeng, Y. Chen, K. Kirschbaum, K. J. Lambright and R. Jin, *Science*, 2016, **354**, 1580.

93 T. Higaki, M. Zhou, K. J. Lambright, K. Kirschbaum, M. Y. Sfeir and R. Jin, *J. Am. Chem. Soc.*, 2018, **140**, 5691.

94 N. A. Sakthivel, S. Theivendran, V. Ganeshraj, A. G. Oliver and A. Dass, *J. Am. Chem. Soc.*, 2017, **139**, 15450.

95 R. Jin and T. Higaki, *Commun. Chem.*, 2021, **4**, 28.

96 M. Zhou, X. Du, H. Wang and R. Jin, *ACS Nano*, 2021, **15**, 13980.

97 S. Chen, T. Higaki, H. Ma, M. Zhu, R. Jin and G. Wang, *ACS Nano*, 2020, **14**, 16781.

98 J. Kim, K. Lema, M. Ukaigwe and D. Lee, *Langmuir*, 2007, **23**, 7853.

99 S. Antonello, T. Dainese, M. De Nardi, L. Perotti and F. Maran, *ChemElectroChem*, 2016, **3**, 1237.

100 S. Hossain, Y. Imai, D. Suzuki, W. Choi, Z. Chen, T. Suzuki, M. Yoshioka, T. Kawakami, D. Lee and Y. Negishi, *Nanoscale*, 2019, **11**, 22089.

101 S. Park and D. Lee, *Langmuir*, 2012, **28**, 7049.

102 S. Hossain, W. Kurashige, S. Wakayama, B. Kumar, L. V. Nair, Y. Niihori and Y. Negishi, *J. Phys. Chem. C*, 2016, **120**, 25861.

103 Y. Song, J. Zhong, S. Yang, S. Wang, T. Cao, J. Zhang, P. Li, D. Hu, Y. Pei and M. Zhu, *Nanoscale*, 2014, **6**, 13977.

104 S. Takano, S. Ito and T. Tsukuda, *J. Am. Chem. Soc.*, 2019, **141**, 15994.

105 T. Higaki, C. Liu, M. Zhou, T.-Y. Luo, N. L. Rosi and R. Jin, *J. Am. Chem. Soc.*, 2017, **139**, 9994.

106 M. Rambukwella, L. Sementa, G. Barcaro, A. Fortunelli and A. Dass, *J. Phys. Chem. C*, 2015, **119**, 25077.

107 P. S. Window and C. J. Ackerson, *Inorg. Chem.*, 2020, **59**, 3509.

108 K. Kwak and D. Lee, *J. Phys. Chem. Lett.*, 2012, **3**, 2476.

109 M. Suyama, S. Takano, T. Nakamura and T. Tsukuda, *J. Am. Chem. Soc.*, 2019, **141**, 14048.

110 K. Kwak, Q. Tang, M. Kim, D.-E. Jiang and D. Lee, *J. Am. Chem. Soc.*, 2015, **137**, 10833.



111 Y. Negishi, K. Munakata, W. Ohgake and K. Nobusada, *J. Phys. Chem. Lett.*, 2012, **3**, 2209.

112 W. Fei, S. Antonello, T. Dainese, A. Dolmella, M. Lahtinen, K. Rissanen, A. Venzo and F. Maran, *J. Am. Chem. Soc.*, 2019, **141**, 16033.

113 L. Liao, S. Zhou, Y. Dai, L. Liu, C. Yao, C. Fu, J. Yang and Z. Wu, *J. Am. Chem. Soc.*, 2015, **137**, 9511.

114 M. Kim, Q. Tang, A. V. Narendra Kumar, K. Kwak, W. Choi, D.-E. Jiang and D. Lee, *J. Phys. Chem. Lett.*, 2018, **9**, 982.

115 S. Hossain, D. Suzuki, T. Iwasa, R. Kaneko, T. Suzuki, S. Miyajima, Y. Iwamatsu, S. Pollitt, T. Kawakami, N. Barrabés, G. Rupprechter and Y. Negishi, *J. Phys. Chem. C*, 2020, **124**, 22304.

116 M. Suyama, S. Takano and T. Tsukuda, *J. Phys. Chem. C*, 2020, **124**, 23923.

117 J. Koivisto, S. Malola, C. Kumara, A. Dass, H. Häkkinen and M. Pettersson, *J. Phys. Chem. Lett.*, 2012, **3**, 3076.

118 K. Nobusada and T. Iwasa, *J. Phys. Chem. C*, 2007, **111**, 14279.

119 L. V. Nair, S. Hossain, S. Takagi, Y. Imai, G. Hu, S. Wakayama, B. Kumar, W. Kurashige, D.-E. Jiang and Y. Negishi, *Nanoscale*, 2018, **10**, 18969.

120 L. Liao, S. Zhuang, P. Wang, Y. Xu, N. Yan, H. Dong, C. Wang, Y. Zhao, N. Xia, J. Li, H. Deng, Y. Pei, S.-K. Tian and Z. Wu, *Angew. Chem., Int. Ed.*, 2017, **56**, 12644.

121 Y. Song, F. Fu, J. Zhang, J. Chai, X. Kang, P. Li, S. Li, H. Zhou and M. Zhu, *Angew. Chem., Int. Ed.*, 2015, **54**, 8430.

122 X. Yan, S. Su, X. Li, S. Jin and M. Zhu, *Dalton Trans.*, 2023, **52**, 4251.

123 H. Deng, Y. Bai, M. Zhou, Y. Bao, S. Jin, X. Li, H. Yu and M. Zhu, *J. Phys. Chem. C*, 2020, **124**, 21867.

124 H. Hirai, S. Takano, T. Nakamura and T. Tsukuda, *Inorg. Chem.*, 2020, **59**, 17889.

125 M. Kim, K. L. D. M. Weerawardene, W. Choi, S. M. Han, J. Paik, Y. Kim, M.-G. Choi, C. M. Aikens and D. Lee, *Chem. Mater.*, 2020, **32**, 10216.

126 S.-S. Zhang, L. Feng, R. D. Senanayake, C. M. Aikens, X.-P. Wang, Q.-Q. Zhao, C.-H. Tung and D. Sun, *Chem. Sci.*, 2018, **9**, 1251.

127 Z. Qin, D. Zhao, L. Zhao, Q. Xiao, T. Wu, J. Zhang, C. Wan and G. Li, *Nanoscale Adv.*, 2019, **1**, 2529.

128 J. Yan, S. Malola, C. Hu, J. Peng, B. Dittrich, B. K. Teo, H. Häkkinen, L. Zheng and N. Zheng, *Nat. Commun.*, 2018, **9**, 3357.

129 Y.-Z. Li, R. Ganguly, K. Y. Hong, Y. Li, M. E. Tessensohn, R. Webster and W. K. Leong, *Chem. Sci.*, 2018, **9**, 8723.

130 X. Kang, S. Chen, S. Jin, Y. Song, Y. Xu, H. Yu, H. Sheng and M. Zhu, *ChemElectroChem*, 2016, **3**, 1261.

131 S. Jin, M. Zhou, X. Kang, X. Li, W. Du, X. Wei, S. Chen, S. Wang and M. Zhu, *Angew. Chem., Int. Ed.*, 2020, **59**, 3891.

132 W.-J. Zhang, Z. Liu, K.-P. Song, C. M. Aikens, S.-S. Zhang, Z. Wang, C.-H. Tung and D. Sun, *Angew. Chem., Int. Ed.*, 2021, **60**, 4231.

133 W. Du, S. Jin, L. Xiong, M. Chen, J. Zhang, X. Zou, Y. Pei, S. Wang and M. Zhu, *J. Am. Chem. Soc.*, 2017, **139**, 1618.

134 Q. Li, J. Chai, S. Yang, Y. Song, T. Chen, C. Chen, H. Zhang, H. Yu and M. Zhu, *Small*, 2021, **17**, 1907114.

135 L. V. Nair, S. Hossain, S. Wakayama, S. Takagi, M. Yoshioka, J. Maekawa, A. Harasawa, B. Kumar, Y. Niihori, W. Kurashige and Y. Negishi, *J. Phys. Chem. C*, 2017, **121**, 11002.

136 C. Cesari, B. Berti, T. Funaioli, C. Femoni, M. C. Iapalucci, D. Pontiroli, G. Magnani, M. Riccò, M. Bortoluzzi, F. M. Vivaldi and S. Zacchini, *Inorg. Chem.*, 2022, **61**, 12534.

137 C. Cesari, T. Funaioli, B. Berti, C. Femoni, M. C. Iapalucci, F. M. Vivaldi and S. Zacchini, *Inorg. Chem.*, 2021, **60**, 16713.

138 I. Ciabatti, C. Femoni, M. C. Iapalucci, G. Longoni, S. Zacchini, S. Fedi and F. Fabrizi de Biani, *Inorg. Chem.*, 2012, **51**, 11753.

139 E. Cattabriga, I. Ciabatti, C. Femoni, T. Funaioli, M. C. Iapalucci and S. Zacchini, *Inorg. Chem.*, 2016, **55**, 6068.

140 T. Kawakami, N. Shimizu, K. Funai, Y. Mitomi, S. Hossain, S. Kikkawa, D. J. Osborn, S. Yamazoe, G. F. Metha and Y. Negishi, *Nanoscale*, 2021, **13**, 14679.

141 S. Hossain, S. Miyajima, T. Iwasa, R. Kaneko, T. Sekine, A. Ikeda, T. Kawakami, T. Taketsugu and Y. Negishi, *J. Chem. Phys.*, 2021, **155**, 024302.

142 W. Kurashige, Y. Mori, S. Ozaki, M. Kawachi, S. Hossain, T. Kawakami, C. J. Shearer, A. Iwase, G. F. Metha, S. Yamazoe, A. Kudo and Y. Negishi, *Angew. Chem., Int. Ed.*, 2020, **59**, 7076.

143 S. Funaki, T. Kawakami, T. Okada, K. Takemae, S. Hossain, Y. Niihori, T. Naito, M. Takagi, T. Shimazaki, S. Kikkawa, S. Yamazoe, M. Tachikawa and Y. Negishi, *Nanoscale*, 2023, **15**, 5201.

144 S. Miyajima, S. Hossain, A. Ikeda, T. Kosaka, T. Kawakami, Y. Niihori, T. Iwasa, T. Taketsugu and Y. Negishi, *Commun. Chem.*, 2023, **6**, 57.

145 D. García-Raya, R. Madueño, M. Blázquez and T. Pineda, *J. Phys. Chem. C*, 2009, **113**, 8756.

146 V. Garcia-Morales and S. Mafé, *J. Phys. Chem. C*, 2007, **111**, 7242.

147 T. Kawakami, N. Shimizu, Y. Mitomi, D. Yazaki, S. Hossain and Y. Negishi, *Bull. Chem. Soc. Jpn.*, 2021, **94**, 2853.

148 T. Kawakami, Y. Mitomi, N. Nishi, R. Kuroasaki, K. Oiwa, T. Tanaka, H. Hirase, S. Miyajima, Y. Niihori, D. J. Osborn, T. Koitaya, G. F. Metha, T. Yokoyama, K. Iida and Y. Negishi, *Nanoscale*, 2023, **15**, 7272.

149 D. Yazaki, T. Kawakami, D. Hirayama, M. Kawachi, K. Kato, S. Oguchi, Y. Yamaguchi, S. Kikkawa, Y. Ueki, S. Hossain, D. J. Osborn, F. Ozaki, S. Tanaka, J. Yoshinobu, G. F. Metha, S. Yamazoe, A. Kudo, A. Yamakata and Y. Negishi, *Small*, 2023, **19**, 2208287.

150 D. Yazaki, T. Kawakami, T. Tanaka, D. Hirayama, Y. Shingyouchi and Y. Negishi, *Energy Adv.*, 2023, **2**, 1148.



151 K. Koyasu and T. Tsukuda, *J. Chem. Phys.*, 2021, **154**, 140901.

152 S. Chen, M. Li, S. Yu, S. Louisia, W. Chuang, M. Gao, C. Chen, J. Jin, M. B. Salmeron and P. Yang, *J. Chem. Phys.*, 2021, **155**, 051101.

153 Y. Lu, Y. Jiang, X. Gao and W. Chen, *Chem. Commun.*, 2014, **50**, 8464.

154 O. López-Estrada, N. Mammen, L. Laverdure, M. M. Melander, H. Häkkinen and K. Honkala, *ACS Catal.*, 2023, **13**, 8997.

